Precision Optical Measurements of DNA Structure and Synthesis

Thesis by

Ziyang Ma

In Partial Fulfillment of the Requirements

for the Degree of

Doctor of Philosophy

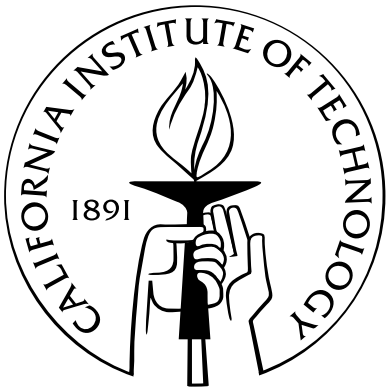

California Institute of Technology

Pasadena, California

2007

(Submitted November 19, 2007)

Acknowledgements

I would like to thank my advisor, Stephen Quake, for introducing me to this highly interdisciplinary field and for giving me the opportunity to work on and learn from different projects. For my projects, Steve was more like a visionary leader who drove the experiments from merely a demonstration to a meaningful level, which in the beginning seemed quite impossible. Steve has constantly urged us to worked harder and read diligently, and I wonder how much more I would have learned or finished if I had always followed his advice.

Jordan Gerton, now a professor, taught me everything on near-field microscopy, and is always available to talk to me and give me good advice, even since he left Caltech. Larry Wade worked with Digital Instruments (DI) to upgrade the open-loop Bioscope to a closed-loop one. Further back, I overlapped briefly with Guillaume Lessard, who developed most of the data acquisition codes.

The carbon nanotube project was done in Pat Collier's lab. Pat was very nice and patient enough to teach me how to use AFM. Ian Shapiro is the one who grew nice carbon nanotubes, and often worked harder than me. That project was very successful, and Larry was even able to persuade the DI people to trade for our techniques. But I regret that we never had enough time and effort to make it work on FANSOM.

At Stanford, I shared the microscope with Jerrod Schwartz (and later on, Stavros Stavrakis), who have been very coordinate and considerate. Jerrod was also a good teacher to me on biochemical issues. Ethan Townsend wrote the LabVIEW program that we use.

I am very grateful to my committee members: professors Pat Collier, Scott Fraser, David Politzer, and Stephen Quake, for taking time to read my thesis.

My most sincere thanks go to the past and current postdocs, graduate students, and visiting scholars in the Quake group. Their pieces of advice and tips, small or big, are deeply appreciated. I cannot list their names here because i am afraid of missing someone.

In the end, I want to thank my family back in China and Jiayao Zhang for their care and support.

Abstract

The structure and synthesis of DNA is important. Traditionally, high-resolution structures are solved with X-ray crystallography, and kinetic measurements are taken with consumption of large amount of reagents. In this thesis, I developed new optical methods to probe the DNA structure and to measure kinetics of DNA synthesis.

I measured the helical rise of A-form DNA at the single molecule level using a near-field optical microscope that has sub-10 nm resolution. The microscope is a combination of an atomic force microscope (AFM) and a fluorescence microscope. Imaging at the single fluorophore level was allowed with the development of a novel phase filter that gives ~ 6 fold improvement in the signal-to-noise ratio. I was able to reliably and repeatedly image pairs of molecules separated by ~ 15 nm and demonstrate the first true Rayleigh resolution test for near-field images.

Various evidences, such as crystal structures and sequencing experiments, indicate that the primer-template DNA sequence may affect nucleotide incorporation. I developed a droplet-based microfluidic fast-mixing device that requires minimal sample consumption and measured kinetics of nucleotide incorporation with DNA sequence permutation. I showed that with careful and systematic kinetic measurements, one can obtain rich information of the process of DNA synthesis.

Contents

List of Figures

Chapter 1

Overview

DNA, the double helix, was discovered in 1953 as a result of modeling [1] and crystallographic imaging[2, 3]. This discovery laid the foundation for modern molecular genetics, and had profound implications for our understanding of basic biology from heredity to evolution. In the cell nucleus, DNA is packed as nucleosomes, which then fold into 30 nm chromatin fibers and further into chromosomes. These packing structures of DNA were recently found to affect gene expression and chromosome stability, serving as carriers of another layer of heredity information [4]. After 50 years of DNA discovery, our understanding of "the secret of life" has only just begun.

To a large extent, biological research is limited by technology. Some important observations and hypotheses cannot be made or tested simply because of the lack of appropriate technology. For example, the nucleosome was discovered in 1974 with X-ray crystallography [5, 6], but its secondary structures, the 30 nm fibers, still remain unsolved [7, 8] because of the lack of imaging methods on that length scale (Fig. 1.1). With the wave nature of light, it is clear, even without rigorous derivation, that the lateral resolution of the optical microscope is limited to about half of the wavelength ($\sim$ 200 nm). X-ray crystallography and nuclear magnetic resonance (NMR), on the

other hand, can have atomic resolution but will only deal with molecules or molecular complexes for which crystals can be formed. Although other microscopy methods, such as cryo-electron microscopy (cryo-EM) and atomic force microscopy (AFM), cover the resolution "gap", they lack chemical specificity.

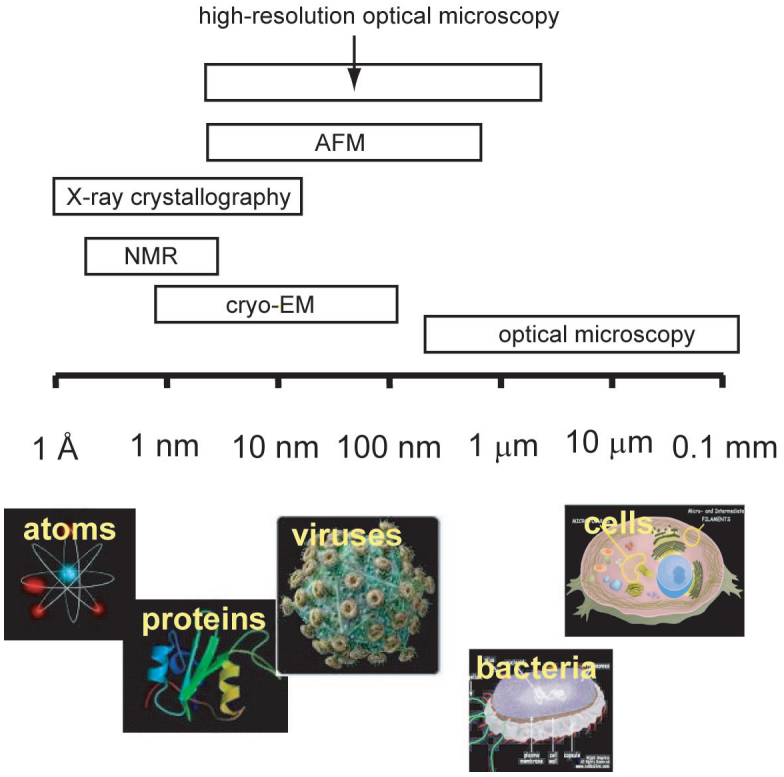

Figure 1.1: Methods map of resolution

Moreover, it is not enough to take snapshots of the molecular complexes along a reaction trajectory. The Arrhenius equation says that a small free energy difference shifts equilibrium significantly; for example, 1.3 kcal/mol would shift the equilibrium constant by one order of magnitude, and it is not possible for X-ray crystallography to resolve such subtle energy changes. In order to predict the outcome of a dynamic process, we have to measure its kinetic parameters. Existing methods, such as stopped

flow and surface plasmon resonance (SPR), suffer from large sample assumption, poor scalability, and sometimes not high enough time resolution. These limitations become more apparent as people start to study how interactions of multiple molecule components give rise to the function of a complex biological system, an exciting emerging field called systems biology.

Drawing on physics and engineering, we wished to push the limit of technologies. We have developed a fluorescence near-field microscope that has better than 10 nm optical resolution, and a microfluidic platform for kinetic analysis, which has minimal sample consumption and allows large-scale parallelization. We were able to measure the helical rise of A-form DNA using the high-resolution fluorescence microscope and study the sequence-context dependence of DNA replication kinetics using the microfluidic fast-mixing chips.

I organized individual projects into independent Chapters, so each is largely self-contained:

- Chapter 2 is an introduction high-Resolution optical microscopy, including both lens-based methods and near-field microscopy.
- Chapter 3 covers fluorescence apertureless near-field scanning optical microscopy (FANSOM).
- Chapter 4 is about fabrication of carbon-nanotube AFM probes. The resolution of FANSOM is ultimately limited by the sharpness of the tip, and carbon-nanotube probes have the potential to offer resolution much higher than silicon

probes.

- Chapter 5 covers sequence dependence of DNA polymerase incorporation kinetics.

- Chapter 6 covers mechanism of droplet formation in microchannels. As I worked on the droplet-based microfluidic fast-mixers, I also studied the mechanism of droplet formation.

Chapter 2

High-Resolution Optical Microscopy

2.1 Introduction

It is a well-known paradigm that the spatial resolution of lens-based optical microscopy can not surpass $\lambda/2$, or precisely,

$$\frac{1.22\lambda}{2nSin(\theta)}. \tag{2.1}$$

Here λ is the wavelength of the light, n is the refractive index, and θ is the aperture angle of the lens. This is because a lens can only focus a propagating wave to a finite-sized spot, called the Airy pattern for circular lenses. For wide field microscopy, this means that photons from features within the spot size would blur on the detector. For scanning microscopy, this means that the propagating excitation laser wave cannot be focused to be smaller than Airy spot in the focal plane, so fluorescent makers within the spot are not resolvable.

Optical microscopy is applied widely in many fields of science, especially biology

and geology. The advantages of non-invasiveness and high chemical specificity, together with the ever-growing spectrum of fluorescent marks, make optical microscopy one of the indispensable tools in biological studies. Many of these studies can be tremendously helped if sub-diffraction limited spatial information is attainable. Near-field optical microscopy and several lens-based methods have been demonstrated to meet this goal. In this section and the following, I will give a brief review of the lens-based and near-field methods.

One of the lens-based methods is to collect hundreds of thousands of photons emitted from a point source, for example, a fluorescent molecule. Although the photons are distributed to a finite area on the detector due to the laws of diffraction, the spatial distribution of photons can be fitted to a gaussian function, and theoretically the center can be determined to arbitrary high precision if there are enough photons. Precision on the order of nanometer was achieved with several millions of photons collected from a fluorophore. Techniques using this method include Fluorescence Imaging with One Nanometer Accuracy (FIONA) [9, 10, 11], Single-molecule High-Resolution Imaging with Photobleaching (SHRImP) [12], Nanometer-Localized Multiple Single-molecule fluorescence microscopy (NALMS) [13], and Single molecule High-Resolution Colocalization (SHREC) [14]. This method has been applied to some niche problems, such as the study of the motor proteins, including myosins and kinesins.

Although the above method provides impressively high precision, it can only locate one molecule per focal spot (or two molecules with much more complicated setup). So

its application is very much limited to some niche problems, such as those mentioned previously. In order to circumvent this limitation, a few groups have investigated much effort in developing methods to simultaneously resolving multiple molecules in a focal spot. One strategy is to "turn on" fluorescent molecule(s) in a small area (smaller than Airy spot) each time. By sequentially turning on different such small areas, one creates a composite image of the sample. Approaches employing this strategy include Stimulated Emission Depletion (STED)[15], reversible saturable fluorescence transitions [16], Photoactivatable Localization Microscopy (PALM)[17], and Stochastic Optical Reconstruction Microscopy (STORM)[18]. For these kind of approaches, resolution as good as 20 nm has been achieved, but the long data acquisition time is considered the limiting factor.

2.2 Near-field Optical Microscopy

Near-field optical microscopy is in the category of scanning microscopy, where the image is taken pixel by pixel with the sample scanned by the laser light. With near-field optical microscopy, the resolution limit of Eq. (2.1) is bypassed as the lens-focused scanning light is replaced by confined light, or optical near fields, that exist near a small aperture or object.

In this section, I will cover physics of near-field optics and introduce two versions of near-field microscopy: near-field scanning optical microscopy (NSOM) and apertureless near-field scanning optical microscopy (ANSOM).

2.2.1 Near-field Optics

I adapt the operational definition of near-field optics from Paesler and Moyer [19]: *near-field optics is the branch of optics that considers configurations that depend on the passage of light to, from, through, or near an element with subwavelength features and the coupling of that light to a second element located a subwavelength distance from the first.*

Macroscopic electrodynamics is quite successful in describing near-field optics. When light waves incident on a nano-scale object, the waves diffract in two portions: the far-field components, which propagate away from the object and can be collected by a lens; and the evanescent near-field components, which are bound to the surface of the object. The existence of the evanescent components at a nano-object can be understood with Fourier analysis. Consider a plane wave incident on a opaque screen with a sub-wavelength aperture Δx: the outgoing wave has components with $k_x > 2\pi/\Delta x \gg 2\pi/\lambda$ (Fig. 2.1); for these components, the propagation vector along the z-axis (k_z,), is imaginary according to the dispersion relation $k_z^2 = k^2 - k_x^2 < 0$, where $k = 2\pi/\lambda$.

Because the evanescent fields bound to the object decay in intensity within a fraction of the light wavelength, they carry information of sub-wavelength fine features. Combined with methods that detect or guide light on a scale much smaller than the wavelength, near-field optics can be exploited for many applications ranging from the development of high recording density of the optical memory systems to high-resolution imaging that circumvents the diffraction limit.

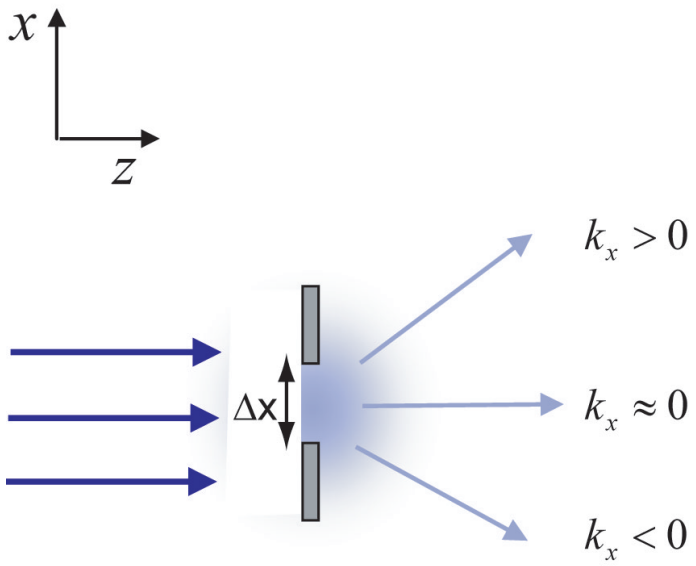

Figure 2.1: Schematics of the origin of evanescent fields. A plane wave passes through a sub-wavelength aperture. The outgoing wave has components with $k_x > 2\pi/\lambda$, for which the propagation vector along the z-axis is imaginary. These components are evanescent.

2.2.2 Near-field Scanning Optical Microscopy

Near-field scanning optical microscopy (NSOM) involves an optical fiber with a small aperture (usually with diameter of 20-200 nm). Laser light is shined through the fiber, and optical near fields exist at the tip of the aperture. This aperture tip raster scans the surface at a close distance, coupling the optical near fields at the tip to the sample. The idea of using near-field optics to achieve sub-diffraction limited was first proposed by Synge in 1928 [20], but was thought to be technically impossible at that time. It is not until 1983 that people were able to make a small enough aperture from an optical fiber, and broke the resolution limit of Eq. (2.1) [21, 22].

Figure 2.2 shows the diagram of NSOM. Resolution at or better than 100 nm is typically achieved with NSOM. However, it becomes more difficult to achieve higher

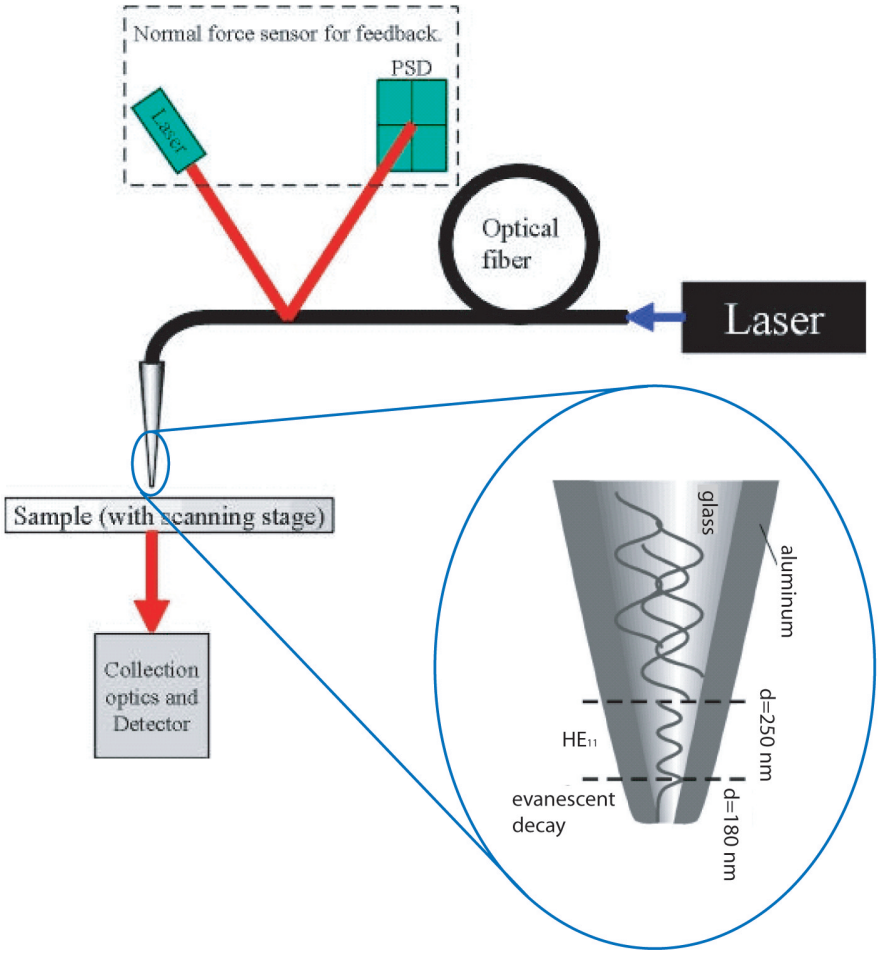

Figure 2.2: The diagram of NSOM (from http://www.nanonics.co.il/main/). The blow up shows mode propagation in the tapered metal-coated optical fiber [23]. The transmission coefficient drops quickly as the size of the aperture decreases. See the text for details.

resolution as the aperture necessarily becomes smaller. For an aperture $d \ll \lambda$, the power throughput, which is defined as the transmitted power divided by the input power, scales with d^4 [24]. For example, if the diameter of the aperture changes from 100 nm to 20 nm, the transmission coefficient drops by 99.8%. The heating of the metal coating is another problem accompanied with low power throughput. Making smaller apertures is not only a technical challenge by itself, but also brings up these

problems. So, the resolution of NSOM is generally limited to 50 nm.

2.2.3 Apertureless Near-field Scanning Optical Microscopy

Apertureless near-field scanning optical microscopy (ANSOM) circumvent the problems of NSOM by using an opaque tip that is externally illuminated. Figure 2.3 shows schematics of ANSOM. The sharp apertureless tip locally enhances the optical fields near it. The resolution of ANSOM closely depends on the sharpness of the tip, which determines the tightness of the near fields.

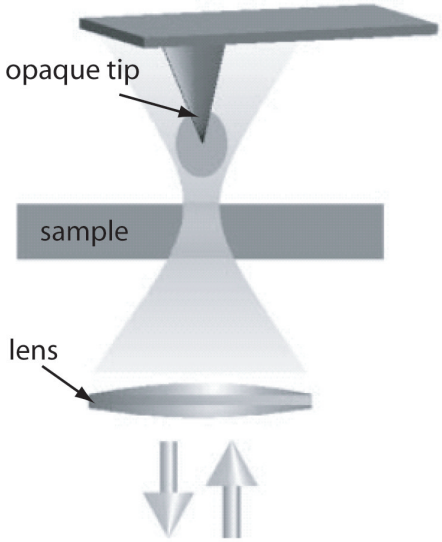

Figure 2.3: Schematics of ANSOM. The focal spot of the external laser is aligned with the tip, and the fields near the tip are enhanced. The tip and the laser can be locked together and scan over the sample give an ANSOM image.

Unlike NSOM, there are no problems of power throughput or probe heating for ANSOM, so the tips can be as sharp as the manufacture technology can afford. Currently, the tips are made by etching directly on a single-crystal silicon wafter (Fig. 2.4). These tips are commercially available and are well characterized in both

tip radius (typically 5-20 nm, depending on the type of the tips) and mechanical properties of the cantilever.

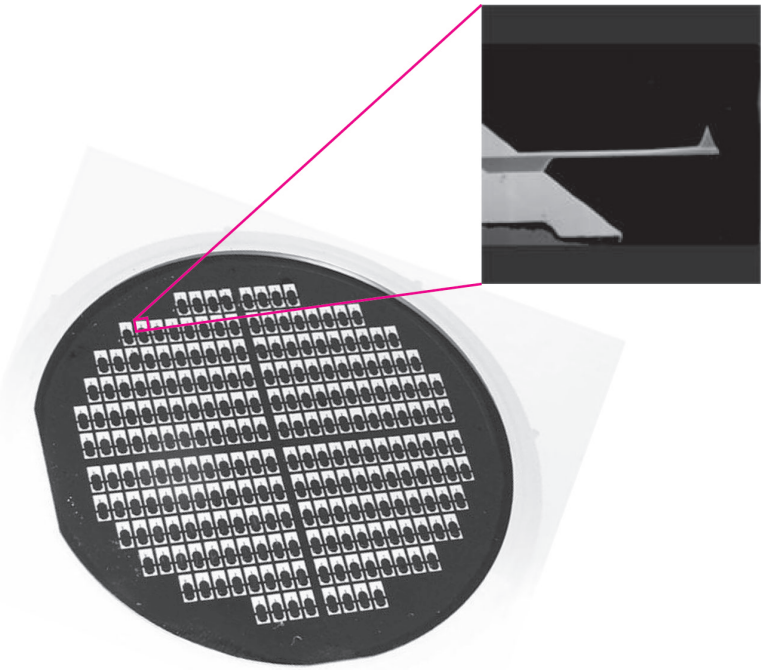

Figure 2.4: A picture of a wafer of commercial tips. These tips are more often referred to as AFM (atomic force microscopy) tips, as they are made for use in AFM. The blow up shows the zoom in picture of the tip and the cantilever.

ANSOM development can be divided into two modules: optimizing the signal to noise ratio and pushing the resolution limit. With well characterized commercial tips, I will cover the first module in Chapter 3, focusing on the development of optics, data acquisition, and analysis. In Chapter 4, I will describe how to manufacture carbon nanotube AFM tips that have with tip radius at 1-2 nm.

Chapter 3

Fluorescence Apertureless Near-field Scanning Optical Microscopy

3.1 Introduction

With the locally enhanced optical near fields at a sharp apertureless tip, near-field imaging with methods of elastic scattering [25, 26], Raman scattering [27, 28], or fluorescence [29, 30] has been demonstrated with spatial resolution at or surpassing 20 nm.

The microscopy developed in the Quake group, called fluorescence apertureless near-field scanning optical microscopy (FANSOM), is for fluorescence near-field imaging. Fluorescence imaging is the most used microscopy method for biological applications because of the chemical specificity and the ever-growing fluorescent markers. Fluorescence near-field imaging has been demonstrated for fluorescent targets including dye-loaded beads [31, 32], quantum dots [30, 33, 34, 35], and single molecules [36, 37, 38], yet none of these previous techniques were able to achieve both single-molecule sensitivity and high-resolution at the same time. More importantly, no

previous ANSOM methods have demonstrated to resolve two close objects, which is a stringent test of resolution and undoubtably relevant to applications.

The failure of the previous methods to achieve both resolution and sensitivity arises from several aspects, such as optics and data analysis, etc. In this chapter, I will describe those aspects and the ways to improve the signal to noise ratio and sensitivity, while leaving the fabrication of high-resolution carbon-nanotube AFM probes to Chapter 4. With the system development and a phase filter that effectively removes the far-field signal excited by the laser illumination, I achieved near-field imaging of fluorescent single molecules at sub-10 nm resolution. I was able to obtain near-field images of single organic fluorophores with very high (≥ 10) signal-to-noise ratio, and thus was able to reliably and repeatedly resolve pairs of molecules separated by $\sim$ 15 nm. The resolving of two close objects presents the first true Rayleigh resolution test for near-field images of single molecules. With near-field imaging, I then measured the helical rise of long (60-bp) A-form DNA oligonucleotides, demonstrating the potential of this technique for biological applications.

In the following sections, I will first discuss the development of system, and then present the results. Much of the content comes from the two published papers in Physical Review Letters [39, 40].

3.2 System Development

In this section, I describe different aspects of system development, from the setup to optics to data analysis, in order to reach the goal of resolving single molecules at

sub-10 nm. I tried to put the subsections in an order with some logical sense, but some subsections are rather parallel to each other, and the order may seem somewhat arbitrary.

3.2.1 Setup

The instrument combines a custom optical layout with a commercial (Digital Instrument Bioscope) atomic force microscope (AFM). Figure 3.1 shows the diagram of the setup.

The excitation laser beam is focused through a glass coverslip and at total internal reflection at the glass-air interface (spot size: 350 × 1000 nm) using a 1.3 N. A. oil-immersion objective lens. The generated evanescent field above the glass interface has a decay length of 120-250 nm. The objective simultaneously collects fluorescence, which is then directed onto an avalanche photodiode through a system of spectral filters (background rejection ratio $\sim 10^{10} : 1$). The focal spot is aligned with the AFM probe by means of a piezoactuated tip-tilt mirror, and the lateral position of the probe is controlled by close-loop feedback. The system has uncorrected residual drift (0.05-0.2 nm/s), which is the dominant source of uncertainty in the probe position.

To obtain enhanced optical near fields at the tip, it is required that the illumination light at the tip has a large polarization component along the tip axis (or vertical to the substrate)[41, 42]. According to analysis of scalar fields, pure polarization vertical to the substrate can be achieved if a beam is at total-internal reflection at the glass-air surface. However, vectorial analysis of the polarization using ray optics shows

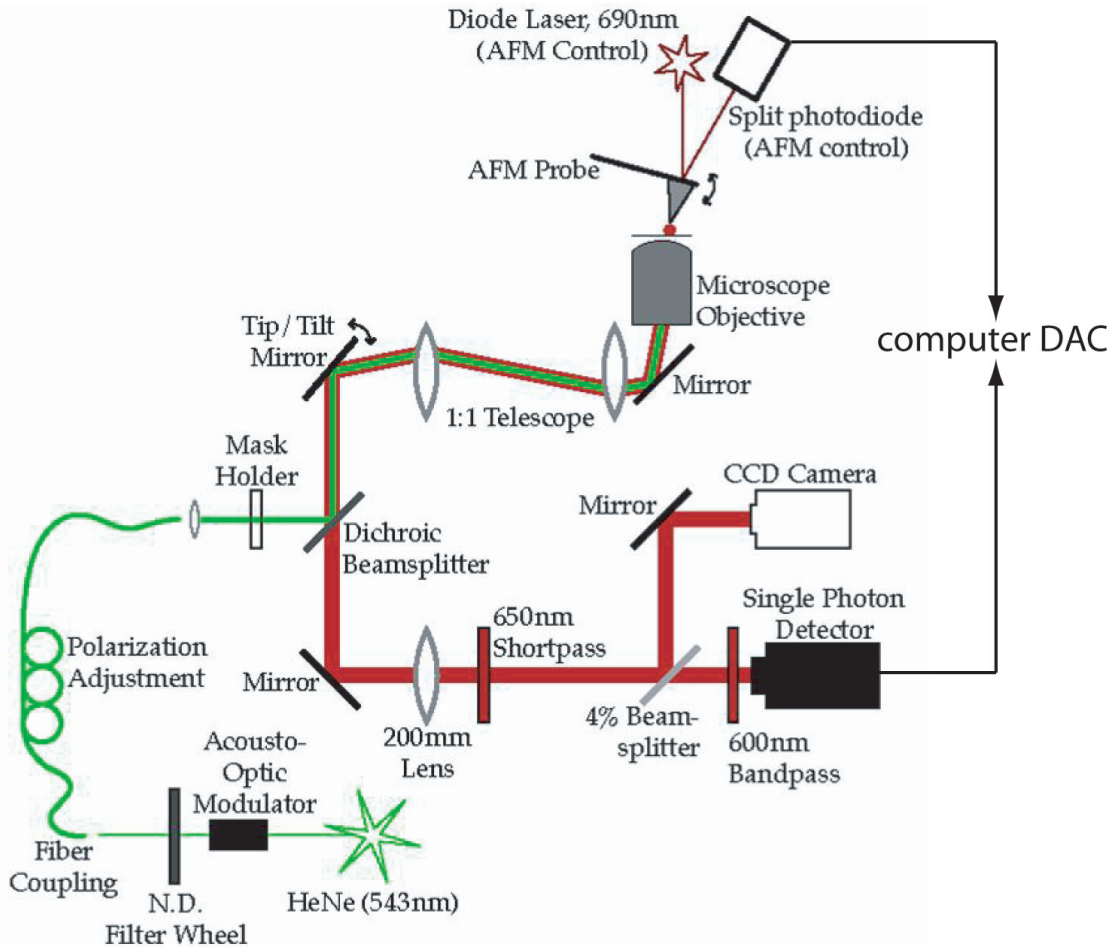

Figure 3.1: Optical setup of FANSOM. The green color and red color code the excitation and fluorescence light, respectively.

that focusing of a symmetric beam yields a small polarization component vertical to the substrate [43] (Fig. 3.2a). Thus, inserting an annular aperture stop (Fig. 3.2b) generates evanescent field on the substrate surface but not a polarization component along the tip axis. To achieve both, a wedged beam-shaping mask (Fig. 3.2c) is inserted into the excitation beam. Another possible way to generate both evanescent fields and a large polarization component along the tip axis is to shift the beam to the edge of the lens; this approach is not adopted in the experiment, however.

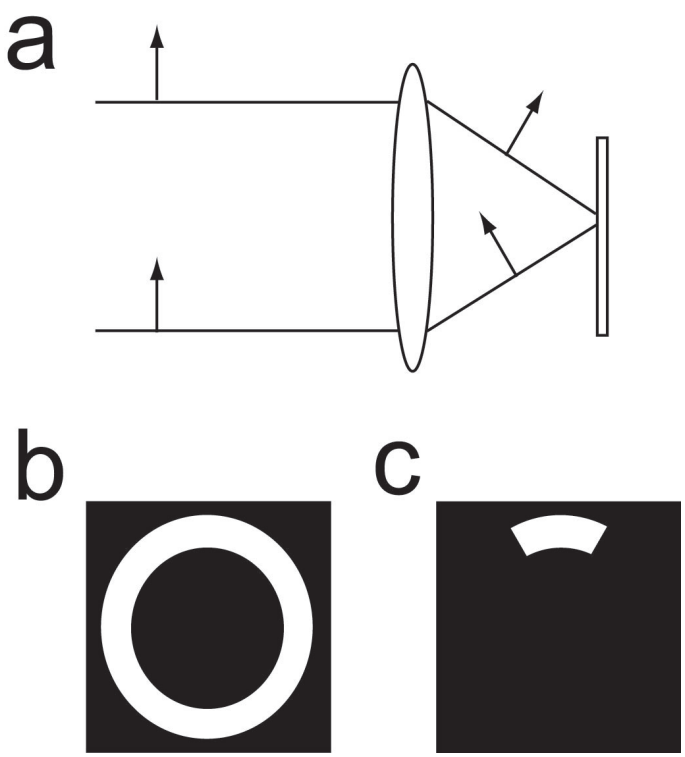

Figure 3.2: (a) Illustration of the geometry of focus in ray optics. (b) A mask for generating an annular beam. Inserting this mask in the excitation beam generates an evanescent field at the substrate surface, but only a small polarization component along the tip axis. (c) A mask for generating a wedged beam. Inserting this mask in the excitation beam generates an evanescent field at the substrate surface with a large polarization component along the tip axis.

Data are recorded to a computer disk in the form of two independent streams of time stamps: one that marks the arrival time of each detected photon, and one that marks a particular phase in each probe-oscillation cycle. Because the raw data are stored permanently in a lossless digital format, multiple analysis algorithms can be applied without degrading the signal.

3.2.2 Data Acquisition

Most of the data acquisition codes was developed by Guillaume Lessard [44]. Here I only describe the use of the time-stamping data acquisition method to fix a hardware problem.

With FANSOM, one obtains AFM topographical image and near-field optical image simultaneously. Both kinds of images enjoy nanometer resolution and give complementary information about the target. One caveat is the uncertainty in correlating the AFM with the near-field image – the two images may be left-right or up-down flipped with respect to each other. The flipping arises because the optical scan the AFM scan synchronize with each other, yet present the images differently. The AFM images are always presented with reference to actual substrate position, while the optical image are reconstructed in a time-sequential manner (earlier data appear on the left/top of the image). The system can not discriminate AFM scan (left-to-right) and recan (right-to-left), and the optical scan may synchronize with either. When the optical scan synchronizes with AFM rescans (right-to-left), the two images are left-right flipped, and when AFM scans in the bottom-to-up manner, the two images are up-down flipped.

To fix the problem, for each AFM image the time stamps of the start/end of each line and the start/end of the image frame are collected. The flipping problem is then fixed with software by comparing the time tags. The method of recording time stamps is a powerful method, and this is just one example of using data acquisition and software to fix a hardware problem.

3.2.3 Dipole Model of the Tip

In the near-field regime, the retardation effects can be ignored. It is then appropriate to take the quasistatic approximation, which considers the temporal oscillation of the fields at $e^{-i\omega t}$ but not the retardation effects. The tip of the probe can be approximated as a sphere with radius r_1 (Fig. 3.3). The scattering of a sphere is a classical problem solved in electromagnetic textbooks: the sphere is equivalent to to a dipole of moment $\mathbf{p}$ placed at the center of the sphere,

$$\mathbf{p} = \varepsilon_2 \alpha \mathbf{E}_0, \tag{3.1}$$

where the polarizability $\alpha$is defined as

$$\alpha = 4\pi {r^3}_1 \frac{\varepsilon_1 - \varepsilon_2}{\varepsilon_1 + 2\varepsilon_2}. \tag{3.2}$$

Here, ε_1 and ε_2 are the dielectric constants of the sphere and the air, respectively.

It is well known that oscillating dipoles radiate, and the field of an oscillating dipole is given by [45]

$$\mathbf{E} = \frac{1}{4\pi\varepsilon_2}\Big(-\frac{\mathbf{p}(t_0)}{r^3} + \frac{3\mathbf{r}[\mathbf{r}\cdot\mathbf{p}(t_0)]}{r^5} + \frac{ik\mathbf{p}(t_0)}{r^2} - \frac{3ik\mathbf{r}[\mathbf{r}\cdot\mathbf{p}(t_0)]}{r^4} - \frac{k^2}{r^3}\mathbf{r}\times[\mathbf{r}\times\mathbf{p}(t_0)]\Big). \tag{3.3}$$

Among the five terms, the first two terms are the fields of a static dipole, the next two terms are induced fields, and the last term is the radiation field, or the far-field

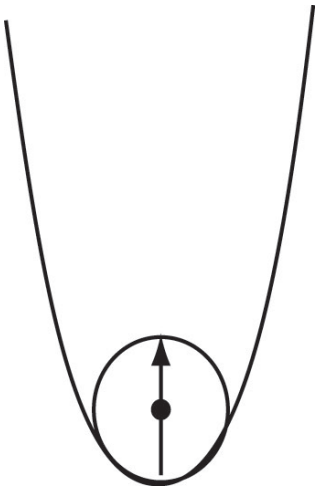

Figure 3.3: Schematics of the AFM probe. The tip of the probe can be approximated as a sphere, whose induced fields outside of the sphere is identical to that of a dipole of moment **p** located at the center of the sphere.

component [46]. In the near-field regime where $r \ll 1/k$, the first two terms dominate:

$$\mathbf{E} = \frac{1}{4\pi\varepsilon_2}\Big(- \frac{\mathbf{p}(t_0)}{r^3} + \frac{3\mathbf{r}[\mathbf{r}\cdot\mathbf{p}(t_0)]}{r^5}\Big). \tag{3.4}$$

This electrostatic dipole model of the tip is also supported by numerical simulations [47] and the experimental measurements described in the following section. The model has been adopted in both fluorescence ANSOM and scattering ANSOM [25, 48]

3.2.4 Characterization of the Optical Near Fields at the Tip

To better understand the advantages of the ANSOM technique and to facilitate development of accurate physical models, it is crucial to rigorously characterize the spatial confinement of the enhancement effect. Previous investigations did not attain the level

of precision necessary to differentiate between various theoretical models [27, 31, 49], and there was no experimental or theoretical consensus regarding either the functionality or the set of parameters governing the spatial resolution [50, 41, 42, 51, 52].

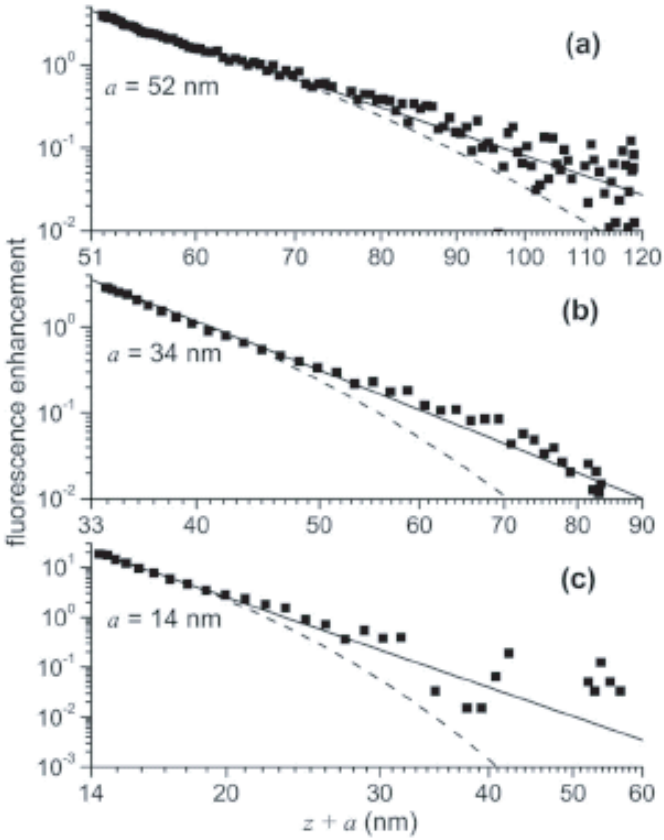

Figure 3.4: Least-squares fit to the approach curve for (a) 20 nm diameter dye-doped sphere; (b) nanorod; and (c) spherical quantum dot. Fits to the power law of Eq. (3.5) (solid curves) and an exponential function (dashed curves) are shown with the data. The horizontal scales are offset by the fitted values of a, and unity is subtracted from the vertical scales.

In this section I describe the determination of parameters that influence the tip-enhanced intensity distribution. Dye-doped spheres and nanocrystals were used in the measurement. The focal spot and AFM probe are centered on an isolated dot,

and the photon and probe-oscillation data streams are recorded for several seconds. A histogram of the phase delay (Δ) between the arrival time of each photon and the preceding probe-oscillation time stamp is computed. Each value of Δ is then mapped to the corresponding value of the tip-sample separation z to produce an approach curve. Figure 3.4 plots each approach curve on a log-log scale. Unity is subtracted from the vertical scales, and the horizontal scales are offset by the fitting parameter a, whose physical relevance is discussed below.

The linear appearance of the data on the log-log scale indicates a power-law decay, and the fluorescence enhancement (ζ) is fit to the function

$$\zeta = \frac{F(z)}{F_\infty} - 1 = \kappa^2 (\frac{a}{z+a})^6, \tag{3.5}$$

where $\frac{F(z)}{F_\infty}$ is the detected fluorescence rate normalized to the background rate (F_∞), and κ is the field-enhancement factor. The solid curves show least-squares fits to Eq. (3.5) (κ, a free parameters), while the dashed curves are exponential decays. The data are clearly consistent with a power law and deviate systematically from the best exponential fit. Previously, both power law [31, 49] and exponential [27] decays were fit to experimental data with equal success. The precision of those experiments was insufficient to differentiate between various models because they did not probe the high-contrast region within several nanometers of tip-sample contact.

The measured $(z+a)^{-6}$ decay corresponds to the "near-field" term in the expression for the field intensity near a point dipole, where z is the distance between the apex of the tip and the sample surface. Thus, in the limit of an infinitesimally small

target particle, the tip-enhanced field is equivalent to a dipole field whose singularity is located within the probe at a distance a from the apex, where a is the tip radius-of-curvature. For finite-sized target particles, the parameter a is a measure of the degree of convolution between the intensity distribution and the excitation-probability distribution, and as expected the fitted values of a increases for larger targets. For smaller targets, a is converging to a value ($\sim$ 10 nm) that is characteristic of the silicon probes used here. This is evidence that the field decay is indeed moderated only by the sharpness of the tip.

3.2.5 Simulation of Near-Field Images

With the electrostatic dipole model of the tip, the amplitude of the total electric field $\mathbf{E}_t(\mathbf{r})$ at the substrate is the sum of the illumination field $\mathbf{E}_{laser}$ and the dipole field,

$$\mathbf{E}_t(\mathbf{r}) = \mathbf{E}_{laser} + \gamma|\mathbf{E}_{laser}|\Big(- \frac{\mathbf{p}}{r^3} + \frac{3\mathbf{r}[\mathbf{r}\cdot\mathbf{p}]}{r^5}\Big), \tag{3.6}$$

where the coordinate origin is at the center of the tip, and γ is a constant that can be derived from experimental measurement. I assume the amplitude of the evanescent illumination field (decay length $\sim$ 100 nm) to be constant.

With the total electric fields, I simulated near-field images. Of particular interest is the simulation images of single molecules, because fluorescent molecules have specific molecular dipole moments and near-field images are a mapping of the electric field to the direction of the molecular dipole moment [36, 53]. For simulation images, the image intensity is calculated as $(\mathbf{E}_t(\mathbf{r})\cdot\mathbf{p}_m)^2$, where $\mathbf{p}_m$ is the dipole moment of the

molecule.

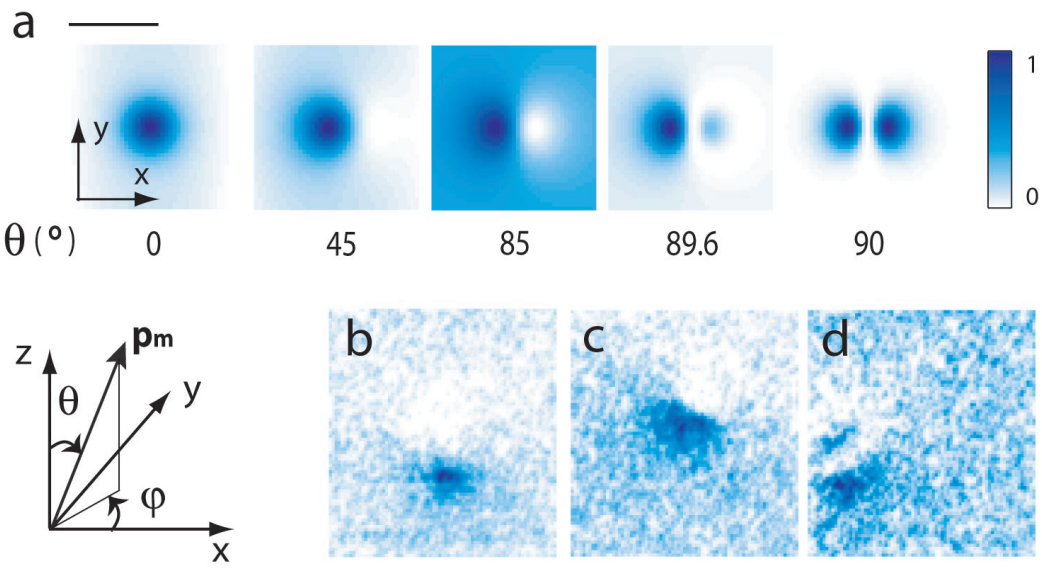

Figure 3.5: (a) Simulation images. The results were simulated with the tip radius at 10 nm and fluorescence enhancement at 5. The scale bar is 20 nm. (b-d) Experimental images (150 nm × 150 nm) showing the patterns similar to the simulated ones for θ close to 90 degrees ($\varphi \neq 0$).

Simulation (Fig. 3.5a) with angle φ shows that as the dipole tilts from the tip axis, the image is elongated, and the center shifts away from the molecular position; for the dipole moment perpendicular to the tip axis ($|\theta - 90°| \leq 0.8°$), the image has two "lobes" side by side with an axis of symmetry through the centers of the two images due to the symmetry of the field; for θ in the range $0.8° \leq |\theta - 90°| \leq 20°$, there is a small region beside the image where the signal is suppressed below the far-field background because the perpendicularity between $\mathbf{p}_m$ and $\mathbf{E}_t(\mathbf{r})$. Since the total field is symmetric about the tip axis, the image for the nonzero φ angle is only a φ-degree rotation of the image for $\varphi = 0$.

These patterns of simulation images provide a good way to check the model of tip.

Indeed, I found experimental results agree beautifully with the simulation images for different molecular dipole moments (Fig. 3.5 b-d). The agreement provides a rigorous support of the electrostatic dipole model of the tip.

The simulation should also help to understand the experimental results, which I will discuss in the following sections. It is obvious that with good signal to noise ratio, the molecular orientation (molecular dipole moment) can be inferred from the shape of the images.

3.2.6 Fluorescence Enhancement

Fluorescence enhancement determines the signal to noise of a near-field image. I have measured fluorescence enhancement for each kind of imaging targets: dye-doped beads, nanorods, quantum dots, and fluorescent molecules. Surprisingly, the measurement shows that fluorescence enhancement depends on the fluorescent targets.

The way of measuring an approach curve has been describe in section 3.2.4. Figures 3.6 and 3.7 show fluorescence enhancement for finite-sized targets and a point-like target (Cy3 molecule). For a finite-sized target, the approach curve is a convolution of the tip-enhanced intensity distribution and the excitation-probability distribution within the target. Thus, the fluorescence decays to half its peak value at larger z for increasing target size: 1.7, 4.3, and 6.3 nm for the quantum dot, nanorod, and sphere, respectively. For a Cy3 molecule ($\leq$ 1 nm), the target size can be neglected, and the fluorescence decay represents the spatial confinement of the tip-enhanced intensity profile.

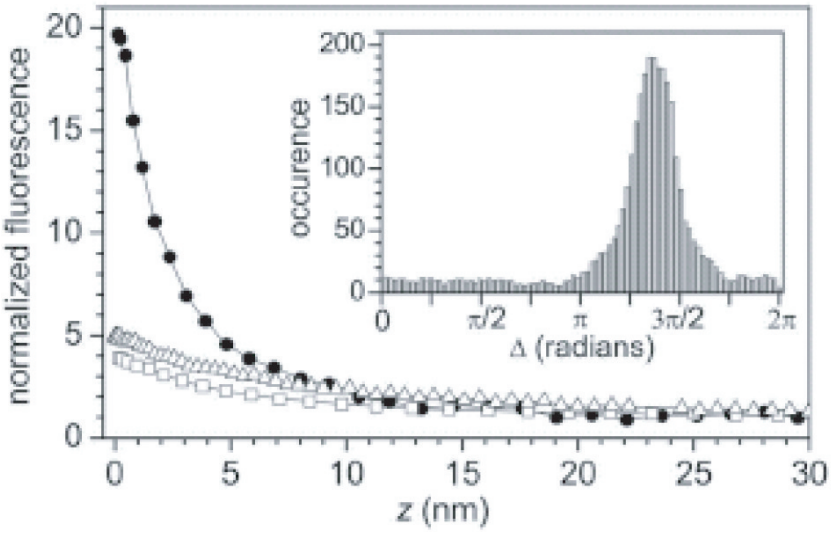

Figure 3.6: Fluorescence enhancement near a sharp silicon probe. Approach curves for a 5 nm diameter dot (solid circles), a 5 × 20 nm CdSe-ZnS nanorod (open squares), and a 20 nm diameter dye-doped latex sphere (open triangles). Additional approach curves extending to $z \sim 150$ nm (not shown) were flat beyond the enhancement region. The vertical scale is normalized to the count rate for a retracted probe. The lines connect the data points. Inset: Histogram of phase delays for the quantum dot.

Interestingly, the half-maximum at at $z = 4$ for a Cy3 molecule is larger than the half maximum for a quantum dot, or close to that of a nanorod. This is actually not surprising. It is well known that the fields near a nanometer-sized object can be enhanced, and due to the same mechanism the fields near an AFM tip is enhanced. The field enhancement effects of the tip and the target then coupled, increasing the maximum fluorescence enhancement. For a quantum dot, fluorescence enhancement ~ 20 has been measured (Fig. 3.6), while for a molecule, only a fold of 2-5 (Fig. 3.7) can be measured.

The small fluorescence enhancement for a molecule gives rise to the problem of poor signal to noise ratio in near-field single-molecule imaging. A method that yields

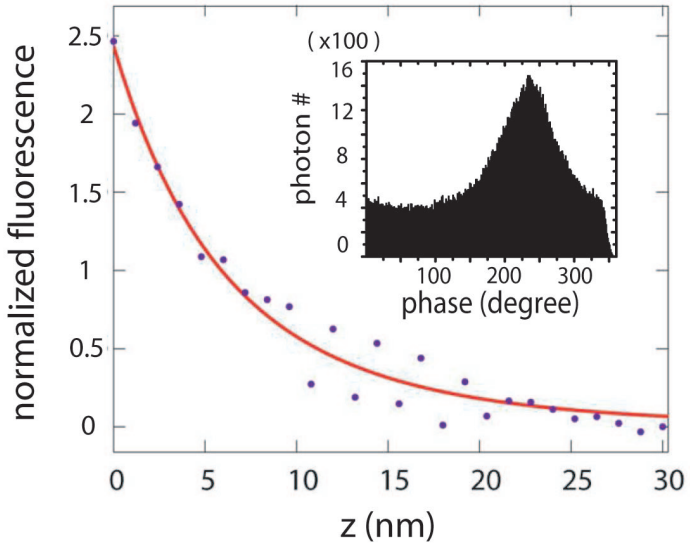

Figure 3.7: Fluorescence enhancement of a Cy3 molecule near a sharp silicon probe. A fluorescence enhancement of 2.5 fold is observed, with the half maximum at $z = 4$ nm. Inset: Histogram of phase delays.

good images of quantum dots may fail to give an image of single molecules.

3.2.7 SNR Improvement by the Phase Filtering Method

With ANSOM, the collected fluorescence signal includes the near-field component excited by the optical near field and the classical far-field component excited by the propagating laser illumination. This problem is more prominent for single molecules, for which the measured fluorescence enhancement is only $\sim$ 2-5 fold (Fig. 3.7 and Fig. 3.8), and the near-field signal is comparable to the fluctuation in the far-field signal (inset of Fig. 3.8).

Although the method of demodulation (Eq. (3.12)) separates the far-field and near-field signals successfully, this method requires large number of photons and is not efficient enough in background suppression (Fig. 3.12). In order to find an

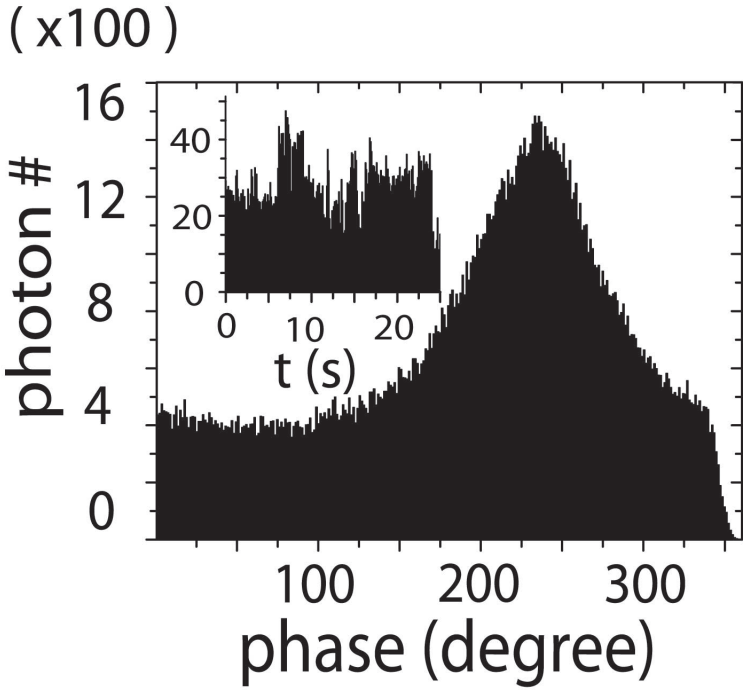

Figure 3.8: Tip-oscillation phase histogram of the photons. The inset is a typical fluorescence time trace of a Cy3 molecule, where the vertical axis is the photon count of 0.01 sec integration time.

efficient method to extract the near-field signal, I studied the 2×10^5 fluorescence photons collected from an isolated Cy3 molecule that was probed by an oscillating tip. The tip-oscillation phase histogram of the collected photons (Fig. 3.8) represents the fluorescence probability of the molecule at different tip-oscillation phases, from which phase ϕ_0, which corresponds to the maximum fluorescence enhancement, can be determined. It was found from experiments that the position of ϕ_0 only depends on mechanical properties of the tip. With the same type of tip, the profile of fluorescence enhancement can be approximated by the function g,

$$g[\phi - \phi_0] = exp\Big(- \frac{|\phi - \phi_0|_p^2}{60^2} \Big), \tag{3.7}$$

where $|\phi - \phi_0|_p$ is defined as $min(|\phi - \phi_0|, |360 - |\phi - \phi_0||)$. The raw near-field signal S_{rn} of a pixel can be calculated as

$$S_{rn} = \sum_{|\phi-\phi_0|_p \leq 60} exp\Big(- \frac{|\phi - \phi_0|_p^2}{60^2} \Big) D[\phi] \tag{3.8}$$

where $D[\phi]$ is the number of photons at phase ϕ. This formula can be interpreted as a bandpass phase filter which passes photons within 60 degrees of ϕ_0 (Fig. 3.8), with weights determined by the enhancement profile g. The 120-degree bandpass window was chosen from testing as an optimum to increase the passed photons and to reduce the bleedthrough between the near-field and far-field signals.

I calculated the far-field signal S_f as

$$S_f = \sum_{|\phi-(\phi_0-180)|_p \leq 60} exp\Big(- \frac{|\phi - (\phi_0 - 180)|_p^2}{60^2} \Big) D[\phi] \tag{3.9}$$

such that molecules outside the near-field volume of the tip contribute equally to S_{rn} and S_f. S_f was then averaged with those of its four neighboring pixels to get $\bar{S_f}$.

The signal of a pixel S_n can be calculated as $S_n = S_{rn} - \bar{S_f}$ for $S_{rn} \geq \bar{S_f}$ and $S_n = 0$ for $S_{rn} \leq \bar{S_f}$.

This phase filtering method effectively suppresses the background noise. Here the background is referred to as area without near-field images. Without considering the weighting for the photons in Eq. (3.8) and (3.9), I can calculate the mean and

variance of the background as

$$\tilde{x} = \sum_{i=0}^{\infty}\sum_{j=0}^{\infty} jP(5i, 5n/3)P(i+j, n/3) \tag{3.10}$$

and

$$\tilde{\sigma}^2 = \sum_{i=0}^{\infty} P(5i, 5n/3)(\sum_{j=0}^{\infty}(j-\tilde{x})^2 P(i+j, n/3) + \sum_{j=0}^{i}\tilde{x}^2 P(j, n/3)), \tag{3.11}$$

respectively, where i and j are dummy variables, n is the background photon number per pixel, and $P(a,b) = (e^{-b}b^a)/a!$ is the Poisson probability density. With the weighting for the photons, the actual standard deviation of the background is $\sigma = 0.75\tilde{\sigma}$. Figure 3.9a plots the calculated background noise (standard deviation) compared to the shot noise, $\sqrt{n}$. The noise suppression provides $\sim$ 6 fold improvement in the signal-to-noise ratio (SNR), making it possible to image multiple fluorescent targets in the focus spot (Fig. 3.9b). Good SNR ($\geq$ 7) can be obtained with up to ten molecules in the focus spot and fair SNR with up to several tens of molecules in the focus spot. In experiments, I calculated the SNR of an image as the difference between the peak pixel signal and the background baseline divided by the background variation, which was calculated as the root-mean-square pixel signal of a 100 nm $\times$100 nm background area. The experimental SNR (see the next section) is in good agreement with the calculation (Fig. 3.9b).

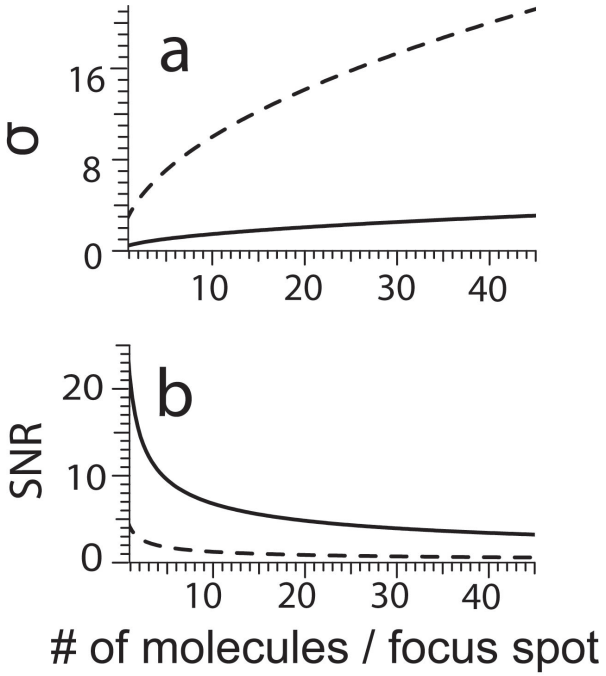

Figure 3.9: (a) The background noise (standard deviation) from the phase filtering method (solid curve) compared with the shot noise, $\sqrt{n}$(dash curve), where n is the number of fluorescence photons per pixel. We assume that on average one molecule emits 10 fluorescence photons per pixel. (b) The SNR calculated as the pixel signal of the near-field image divided by the background noise from the phase filter (solid curve) and by the shot noise (dash curve). For the solid curve, the pixel signal of the image is $0.60fN/3$ (f: fluorescence enhancement factor; $N = 10$: the number of photons per pixel emitted by a molecule) according to Eq. (3.8), which is the weighted sum of the near-field photons. For the dash curve, the pixel signal of the image is the $0.75fN/3$, which is the direct sum of the near-field photons (Fig. 3.8). For both curves, we used $f = 5$

3.2.8 SNR Improvement by Minimization of the Focus Spot

The signal to noise ratio (SNR) of an image decreases as more fluorescent targets are in the laser focus because all the fluorescence photons from these targets are collected by the detector, and only a small portion of the photons are emitted by targets that are excited by the tip-enhanced field. Figure 3.9b (dash line) shows the calculated SNR with different number of targets in the focus spot.

With the same target density, minimizing the size of the focus spot decreases the number of targets in the focus spot, thus improves SNR. Another advantage of smaller the focus spot is alleviation of photobleaching of the fluorescent targets, which is especially important for single molecules.

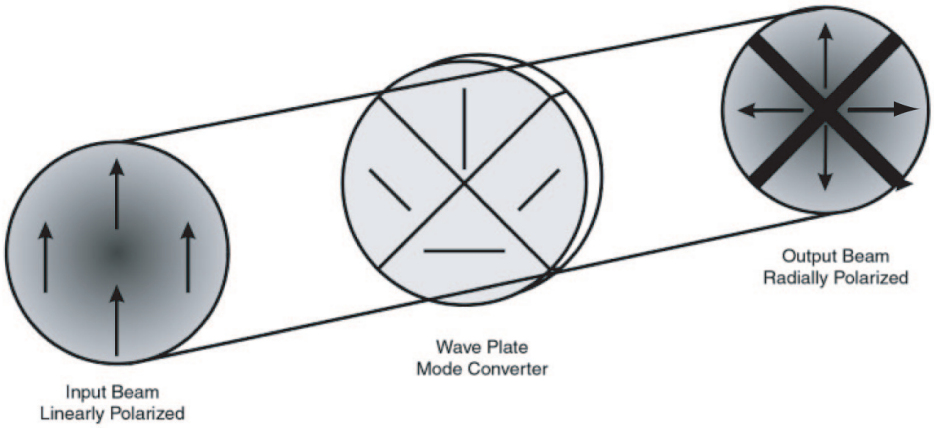

Figure 3.10: Schematics of the mode converter that changes a beam from linear polarization to radial polarization. The mode converter can be made by placing 4 quadrature of wave plates together as depicted.

It has been experimentally demonstrated that a radially polarized beam can be focused to a spot (0.16 λ^2) significantly smaller than for linear polarization (0.26 λ^2) [54]. This can be understood from the vector properties of light (see Fig. 3.2a for reference): after focused by a high numerical aperture (with an annular aperture), the electric field vectors for a radially polarized field are essentially parallel to the optical axis and interfere perfectly. It was also demonstrated that, with an annular aperture, the electric field at the focus of a radially polarized beam is mostly longitudinal. A radially polarized field thus provides the ideal mode to be used in ANSOM. Figure 3.10 shows the schematics of converting a linearly polarized beam into radial polarization.

3.3 Results

3.3.1 FANSOM of Dye-loaded Beads

Dye-doped beads are very good fluorescent samples for FANSOM because they are bight and stable (no photobleaching during imaging). The beads are so robust that nothing can go wrong during sample handling, so they are the ideal control sample for FANSOM. Before imaging other fluorescent samples such as quantum dots and single molecules, I always take an image of an 20 nm diameter dye-doped beads. If FANSOM fails to give a near-field image for a bead, it is always something goes wrong with the system. To trouble shoot, I usually start checking from AFM and alignment.

3.3.2 FANSOM of Nanocrystals

Nanocrystal samples were prepared by drying a dilute solution of CdSe-ZnS core-shell quantum fots onto a clean glass coverslip. The dots have a mean diameter of ~ 5 nm and an emission spectrum centered near $\lambda = 600$ nm. The fluorescence rate is highly dynamic, exhibiting "blinking" and sudden change in quantum yield (QY), in agreement with previous observations [34, 55, 56]. When a quantum dot is "on" and in a high QY state, a typical count rate of $\sim 2 \times 10^4$ sec^{-1} is measured with ~ 300 nW of illumination power.

A demodulated fluorescence image of a nanorod is shown in Fig. 3.11a. The image was generated by raster scanning the AFM probe at a rate of 4 lines/s and then dividing each line into spatiotemporal pixels. These scan rates are at least 5

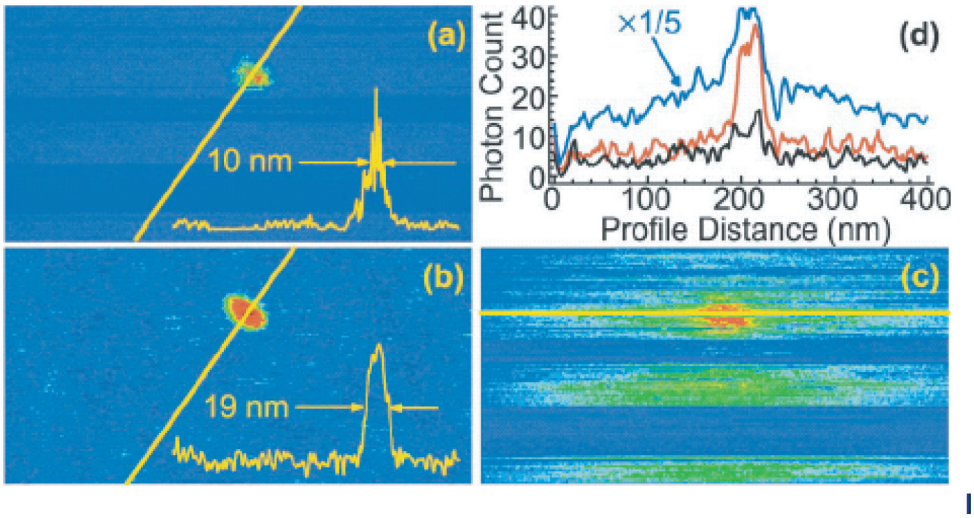

Figure 3.11: Near-field fluorescence image of a nanorod. (a) Fluorescence demodulation signal. (b) AFM probe height (5 nm at peak). (c) Total photon count. Insets in (a) and (b) show signal profiles along the designated axis of length 250 nm. Blue curve in (d) shoes the total photon count ($\times 0.2$) along the horizontal axis in (c), while red and black curves show the photon count within two ranges of tip-sample separation: $0 \leq z \leq 0.4$ nm (red) and $2.5 \leq z \leq 4.5$ nm (black). Field-of-view is $400 \times 200nm$: 256 lines of 1024 pixels each.

times faster than previous work for one-photon fluorescence [31, 34, 35] and 10 times faster for both two-photon fluorescence [29] and Raman scattering [27].

As nanocrystals have strong fluorescence ($\sim 2 \times 10^4$ sec^{-1}), pixel values are simply computed as the component of the photon-time-trace's Fourier power spectrum at the probe-oscillation frequency

$$P = \left(\sum_i sin\Delta_i \right)^2 + \left(\sum_i cos\Delta_i \right)^2, \tag{3.12}$$

where Δ_i are the measured phase delays, and the summation is over all detected photons for the given pixel. When the probe is in the lateral vicinity of the target, the

Δ_i are biased toward the phase value of tip-sample contact, where the fluorescence rate is maximally enhanced. Otherwise, the Δ_i are uniformly distributed, and P vanishes to within the shot noise. Comparing Figs. 3.11a and 3.11b shows that the spatial resolution of the demodulated image is comparable to the tip sharpness and surpasses even the AFM resolution. Comparing Figs. 3.11a and 3.11c demonstrates the effectiveness of the demodulation method.

Figure 3.11d shows three signal profiles along the horizontal axis indicated in Fig. 3.11c corresponding to the summation of photons over the entire probe-oscillation-cycle (blue), within a tip-sample separation range of $0 \leq z \leq 0.4$ nm (red), and $2.5 \leq z \leq 4.5$ nm (black). Here, horizontal profiles are chosen to avoid the regions of quantum-dot blinking. Nearly 20% of the detected photons are emitted when the tip apex is within 0.4 nm of the sample surface (red curve), even though this corresponds to only $\sim 3\%$ of the oscillation period. The black curve approximates the typical scanning conditions of previous ANSOM experiments, which maintained a tip-sample gap roughly in this range [31, 34, 35]. Clearly, those conditions yield both inferior contrast and resolution compared to our technique.

Figure 3.12 shows a fluorescence demodulation image of spherical quantum dots in false-color relief. The arrows indicated the measured FWHM for two dots and suggest a spatial resolution of ~ 8 nm for the smaller one.

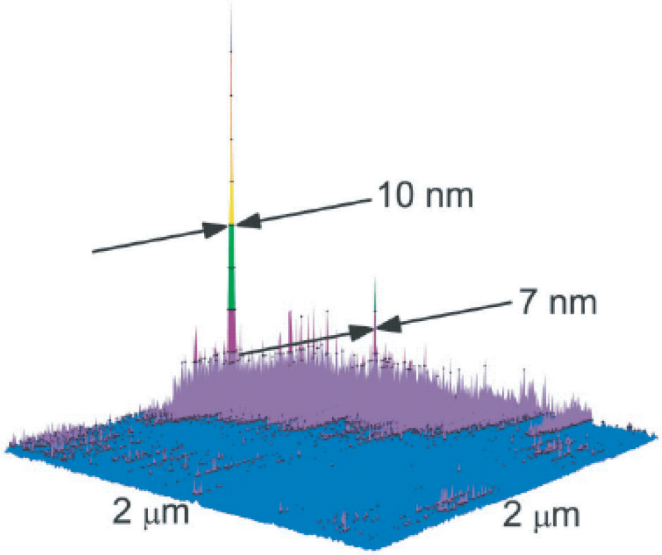

Figure 3.12: Near-Field Image of Quantum Dots. The degree of contrast is emphasized by false-color relief. The image contains 512 lines of 1000 pixels each. The arrows indicate the measured FWHM for two quantum dots.

3.3.3 FANSOM of Single Molecules

Single-molecule near-field imaging has intrigued scientists since the first demonstration of single-molecule near-field images at sub-diffraction limited resolution by Betzig at al. [36]. Single molecules are widely used as fluorescent tags or reporters in biology [57] and sensitive probes in materials and physical chemistry [58]. They are also model single quantum systems for studying light-matter interactions that has led to observation of new physical effects [58].

Although ultrahigh spatial resolution has been demonstrated with ANSOM, it has been a challenge [59, 60, 61] to image fluorescent single molecules due to the inherent molecular fluorescence fluctuation (inset of Fig. 3.8) and the significant shot noise accompanying the limited number of photons available before photochemical destruction (photobleaching) of the molecule. Two experiments achieved resolution

at 30 - 40 nm by imaging isolated molecules in vacuum, in a matrix that reduces photobleaching [38], or by using nanofabrication to form a metal tip on top of a fiber aperture in order to reduce the background [37]. More recently, novel "nanoantennas" probes [62, 63, 64] were shown to hold promise for imaging single molecules.

By using the phase filtering method described in the previous section, I was able to image single molecules using commercial AFM probes in ambient air.

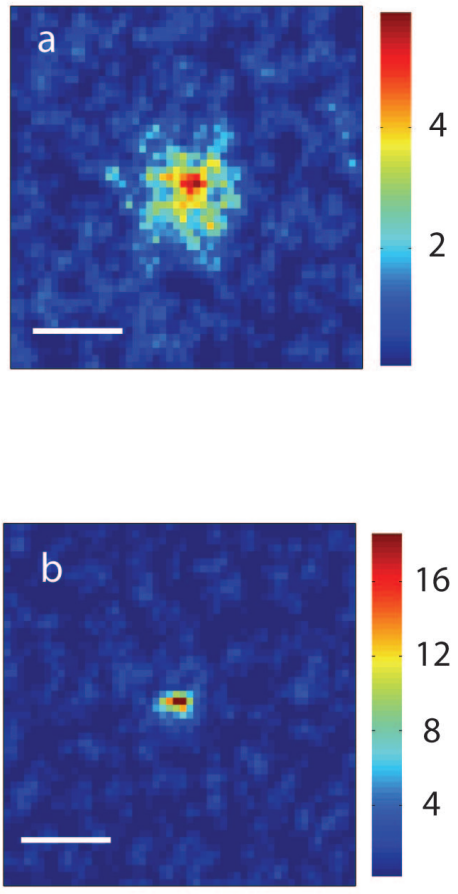

Figure 3.13: Near-field images of Cy3 molecules. Each figure was extracted from a 1×1 μm, 512×512pixel image. The SNR is 16.2 and 25.5 for image (a) and (b) respectively. Both scale bars are 25 nm.

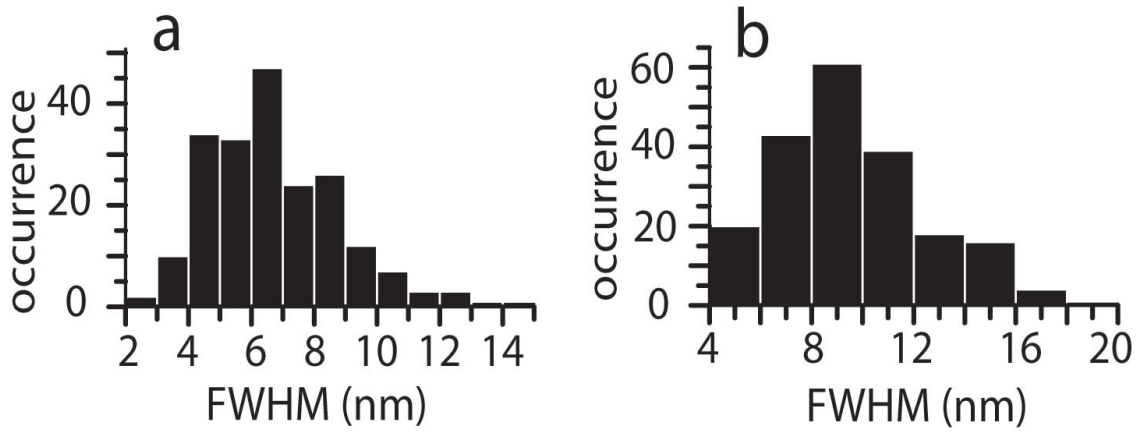

Figure 3.14: Histograms of FWHM measured along the minor and major directions, respectively. The average FWHM is 6.8 nm and 9.6 nm, respectively

I imaged 211 isolated single Cy3 molecules. The near-field images are either symmetric (Fig. 3.13a) or elongated in one direction (Fig. 3.13b) due to different dipole orientations, which will be discussed below. The histograms of full width at half maximum (FWHM) measured along the minor and major directions of all the 211 images are shown in Figs. 3.14a and 3.14b, with the average at 6.8 nm and 9.6 nm, respectively. Compared to bulk samples, single-molecule images are highly variable because of the random dipole orientation. It is clear that simply choosing the linewidth of a single image is not an accurate method for determining resolution. Here we define an average resolution of 8.2 nm, which is $\sim$ 3-4 times better than the previous best ANSOM measurements and close to an order better than typical results of apertured near-field microscopy.

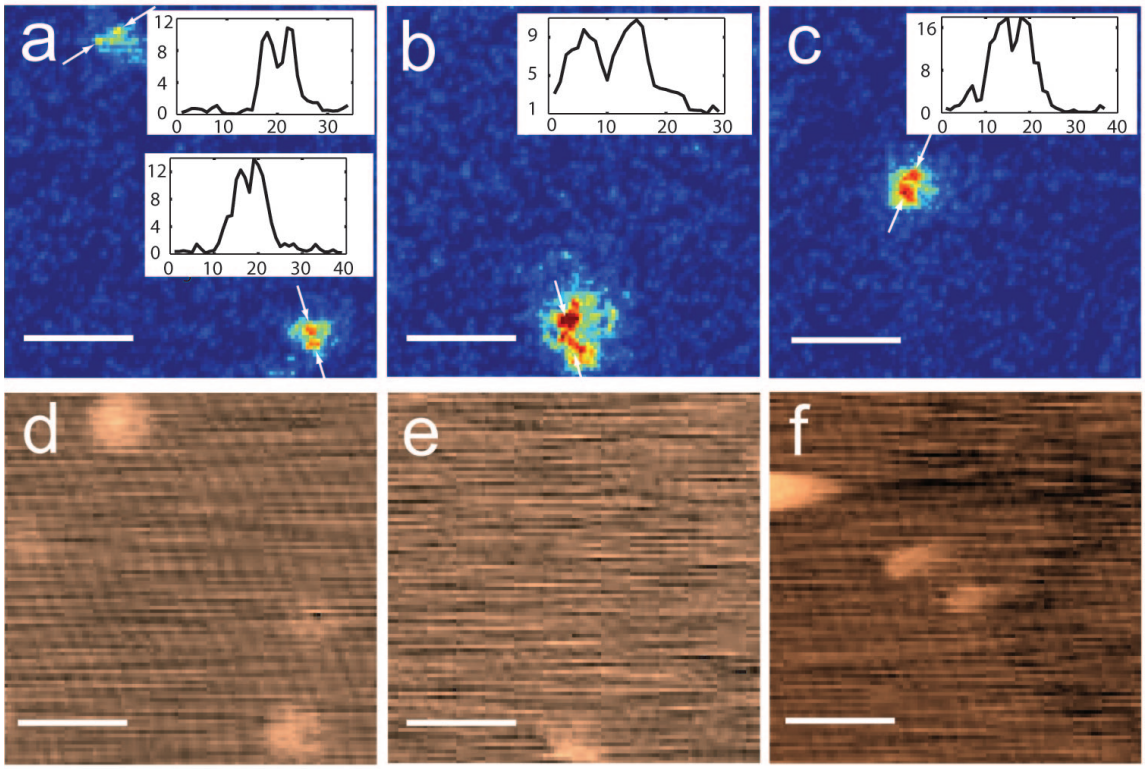

Figure 3.15: (a) - (c) Near-field images of Cy3 pairs. Each figure was extracted from a 1×1 μm, 512×512 pixel image. For each pair of images, the profile with the line cut through the two image centers (indicated by arrows) is shown in the inset, where the horizontal axis is the distance in pixels (1.95 nm/pixel), and the vertical axis is the pixel signal. The SNR is 12.4 and 15.9 in (a), 16.1 in (b), and 20.4 in (c). (d) - (f) The topological AFM images corresponding to near-field images (a) - (c), respectively. All the scale bars are 50nm.

3.3.4 Resolving Two Close Molecules

Measuring true resolution has long been a challenge in near-field microscopy; one of the strongest tests is to make a "Rayleigh" type resolution measurement, in which two proximate point sources are resolved from each other. To my knowledge, there have been no such rigorous near-field measurements made with single molecules, which are excellent approximations of a point source. With the effective phase filter, I was able to resolve two Cy3 molecules linked by a 60bp double-stranded DNA oligonucleotide.

Figures 3.15 a - c are the near-field optical images of such molecule pairs, where Figs. 3.15 d - f are the corresponding topological AFM images. It is clear that ANSOM has better resolution than AFM even with the same tip because the force involved in AFM, which is proportional to the inverse of the tip-sample distance for pyramidal tips [65], decays much more slowly than the optical near field at the tip. There are no previous AFM experiments that resolved DNA molecules as short as 15 nm; instead, round images for short DNA molecules were observed in this (Fig. 3.15d) and previous experiments [66].

I imaged a total of 389 double-stranded DNA oligonucleotides, 29% of which showed resolvable Cy3 pairs. The Cy3 labeling efficiency for each strand is about 80%, so I expect that 67% of the optically detectable DNA oligonucleotides are actually labeled with two Cy3 molecules. Factors such as imperfect annealing, photobleaching of one of the Cy3 molecules, and worn tips can all contribute to the failure to resolve the rest. As a control experiment, the 211 images of single Cy3 molecules were analyzed in the same fashion, and double-lobed artifacts were found in only 4% of the images (Fig. 3.16b), a substantial improvement over other methods which have such artifacts in all images [37].

3.3.5 Measurement of the Helical Rise of A-form DNA

With the two Cy3 molecules at each end resolved, the end-to-end distance of 60bp A-form DNA can be measured. Although the image can shift from the actual position of the Cy3 molecule (Fig. 3.5a), and the image center can only be determined at finite

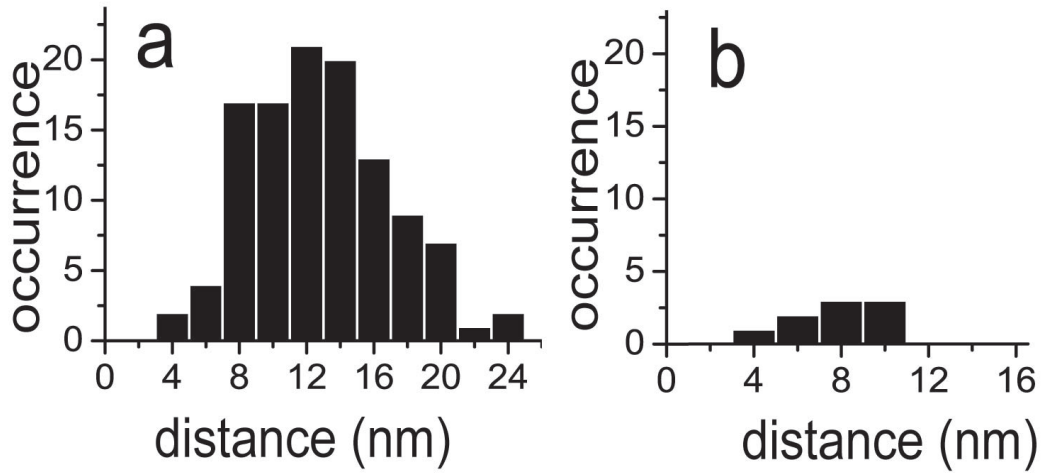

Figure 3.16: (a) The histogram of distances measured between the centers of each image pair. (b) The histogram of distances between the two artifactual lobes of isolated Cy3 molecules.

precision with the limited number of photons, these are random factors which average out over multiple measurements. I measured the distance between the two image centers of each pair and the histogram is shown in Fig. 3.16b. The statistical result of the 113 measurements is 13.0 nm $\pm$ 4.1 nm (standard deviation), with standard error of the mean $\sigma_\mu = 0.4$ nm. The flexible carbon linker ($\sim$ 0.6 nm) between the Cy3 molecule and DNA may also contribute to the distribution of the measurements, although there is evidence that in liquid Cy3 will stack at the immediate end of the DNA molecule [67]. However, systematic error exists in the experiments. Simulation shows that for tip radii above 10 nm, the two images shift closer because the tip enhances both molecules when it is in between the two molecules; for example, a shift of 2.5 nm was simulated for two molecules separated by 15 nm with a tip radius of 15 nm. The shift increases with the tip radius and is difficult to estimate due to tip wearing during the process of imaging, although the linewidth of the majority of the

images indicates a tip radius below 15 nm. Therefore, the precision in determining the length of the DNA has a statistical error of 3% and systematic error up to 20%, depending on the sharpness of the tip.

DNA structure depends strongly on humidity and takes the A-form and B-form structure at low and high humidity, respectively [68]. It is now understood that DNA-binding drugs and proteins can induce local conformational conversion between the two structural forms [69]. In our experiments the DNA molecules are imaged in an environment of $\sim$ 30% humidity that is well below the 73% threshold between A-form DNA and B-form DNA. An unresolved paradox in X-ray diffraction studies of A-form DNA is that fibers of long DNA molecules with mixed sequences yield a consistent value of 2.6 Å/bp for the helical rise [70], but crystal structures of small oligoucleotides ($\sim$ 10bp) with well defined sequences reveal an average value of 2.83 Å/bp with substantial variation across different sequences (standard deviation $\sim$ 0.36 Å/bp) [71]. The source of the discrepancy is as yet unresolved, although crystal artifacts, molecular weight effects, and incomplete sequence sampling may all play a role. It is also known that the DNA structure of a single sequence can vary within a crystal, depending on a variety of external factors [72]. Our fluorescence ANSOM measurements described above allow an independent determination of the helical rise and do not suffer from artifacts due to crystal packing or small molecular weights. The result (2.17 Å/bp) agrees with the x-ray data of fibers within one sigma of our largest estimated experimental error and falls within the two sigma limit of the sequence-dependent variation in the helical rise observed in crystal structure data.

3.4 Future Improvements

The phase filtering technique should also be applicable to "nanoantennas" [62, 63, 64] and supersharp probes with tip radii at 1-2 nm such as single-walled carbon nanotube AFM probes [73, 74] and diamond-like spike probes (Veeco Instruments). With advances in probe technology, both the systematic error and the spatial resolution of ANSOM can be improved, and it should be possible to obtain high resolution structural information on macromolecular complexes by averaging pairwise or higher order measurements over many molecules and by making measurements over samples that have been labeled in different locations, much as cryoelectron microscopy reconstructs images by averaging over many projections. ANSOM is closely linked to advances of AFM technology such as imaging in water and fast frame imaging speeds [75], and it may ultimately be possible to combine optical resolution approaching that of electron microscopy with the ability to image molecules in physiological conditions.

Chapter 4

Carbon Nanotube Tips

4.1 Introduction

Single-walled carbon nanotubes (SWNT) have shown great potential as high-resolution AFM imaging probes [76, 77, 78]. The level of resolution possible for FANSOM is ultimately limited by the sharpness of the tip. Commercially available silicon probe tips have radii of curvature of 5-15 nm, but they are very delicate, with substantial variation in tip shape and size even between successive images. On the other hand, SWNTs typically have diameters between 1.5 - 6 nm and are chemically and mechanically robust. The axial Young's moduli is about 1.25 TPa [79, 80], so the tip structure should be stable over prolonged imaging periods [81]. SWNTs can also be functionalized at their ends, permitting a broad array of applications [82]. However, it is difficult to reproducibly assemble large quantities of high-quality SWNT AFM tips. I will describe the method we developed for reliably fabricating SWNT AFM tips. Much of this chapter is extracted from our paper published in Nano Letters in 2004 [74].

4.2 The Fabrication Method

Successfully fabricating a probe suitable for AFM imaging in air involves several steps: attaching the nanotube to a silicon AFM tip, shortening it sufficiently to enable high resolution imaging, characterizing its quality, and sorting it for later use. We compared several methods for attaching nanotubes to silicon AFM tips: manual assembly [83], direct growth [84, 85, 86], and pickup. Manual assembly of AFM probes was found to be relatively simple, but the nanotubes had to be large enough to be seen and manipulated under the optical microscope, and thus did not yield high-resolution probes [83]. While direct growth [84, 85, 86] offers the potential for parallel fabrication, we found the yield was quite low. Therefore, we focused our efforts on the pick-up technique.

4.2.1 Carbon Nanotube Growth

The first step of the procedure is to grow carbon nanotubes on a substrate. We grew SWNTs via chemical vapor deposition (CVD) on 4 mm to 8 mm square, 500 μ m thick p-doped Si wafers. Four different methods were used to coat the substrates with iron catalyst: spin coating a solution of $Fe(NO_3)_3 \cdot 9H_2O$ in isopropyl alcohol [73], thermal evaporation of iron onto the substrate, electron beam evaporation of iron onto the substrate, and incubation with ferritin. We achieved the most uniform deposition of small (1-2 nm) catalytic sites with high spatial density by using ferritin-derived iron nanoparticles, prepared as described by Dai and co-workers [87].

CVD growth was performed in a 22 mm inner diameter Lindberg/Blue M quartz

tube furnace with a single heating zone 312 mm long, as shown in Fig. 4.1. Five wafers are positioned 12.5 mm apart in a specially designed quartz holder, oriented vertically and with the catalyst-coated side facing away from the direction of the incoming gas. A significant advantage of this holder is that it enables up to three small substrates to be mounted side-by-side in each slot for parallel comparison of growth results under nearly identical temperature and gas flow conditions.

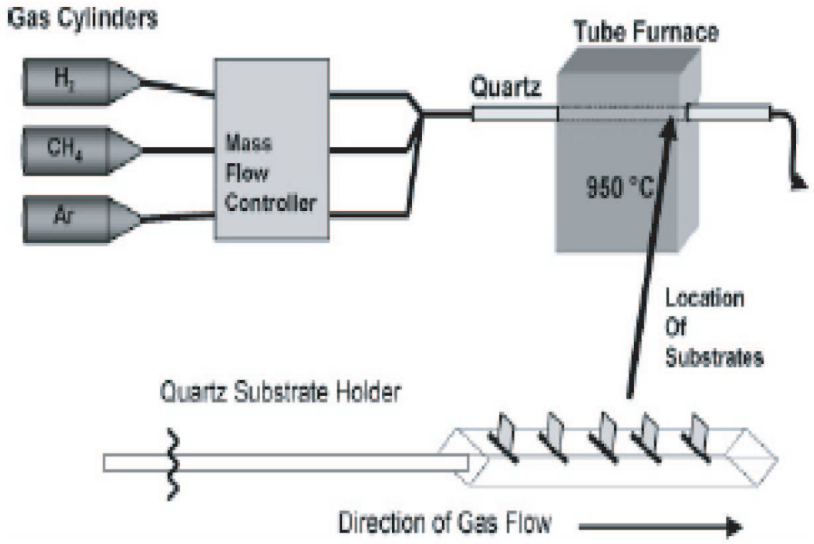

Figure 4.1: Diagram of chemical vapor deposition (CVD) apparatus for growing carbon nanotubes.

We found that growth was faster (5 μm long nanotubes within one minute) and the distribution of tube lengths increases when the catalyst-coated surface was facing away from the incoming gas flow. This is probably due to increased turbulence the gas flow at the catalyst coated side after passing over the edges of the substrate.

Induced turbulence should minimize the role of diffusion-limited growth relative to nucleation rate in the growth kinetics, but at the expense of uniform growth. SWNTs on the substrate vary in diameter from 1.6 to 3.0 nm, and length from 100 nm to 5 μm, as imaged by AFM and SEM.

The distribution of tube diameters varied with the size of the catalytic sites. For example, we found that spin coating many drops of dilute solution of the iron nitrate catalyst to give a high density of small catalytic sites gave a slightly broader tube diameter distribution than did ferritin. In contrast, depositing a few drops of higher density iron solutions yielded broad size distributions and larger average tube diameters. Based on AFM analysis of these substrates, it appears that the larger tube diameters resulted from larger catalytic sites on the substrate.

4.2.2 Carbon Nanotube Pick Up

The pick-up technique, developed by Lieber at al., is an efficient and consistent method for mounting SWNT in the proper orientation. When SWNTs are grown on a flat substrate, a small percentage of the tubes are orientated vertically and can be picked up when the AFM tip scans scross the surface in tapping mode. The nanotube binds to the side of the pyramidal AFM tip via attractive van der Waals forces, and usually remains attached firmly such that it can be repeatedly pressed into and scanned across the substrate surface. We found that it was important to reduce the field of view (from 10 μm to 10 nm) or retreat the tip as soon as a nanotube was successfully picked up in order to minimize the probability of picking up additional

tubes.

It is also important to note that the ambient humidity appears to affect the efficiency of the pickup method. We found it nearly impossible to pick up nanotubes under high humidity conditions. Enclosing the AFM in a glovebag under a flow of dry nitrogen for about 30 mins rejuvenated the process. There are two possible explanations for that. First, at higher humidity, it is harder to overcome capillary forces due to the build up of a surface layer of water on the substrate. Second, increasing water build up on the tip decreases the attractive interactions between the nanotube and the AFM tip. It is known that the van der Waals interactions between the nanotube and AFM tip surface are not strong enough to keep the tube attached to the tip in water [73].

The long-term stability of pickup substrates appears to vary depending on how they were prepared. Ferritin and ferric nitrate substrates appear to be substantially less effective for pickup attachment after 4 to 6 months. It is probably due to the weak mechanical attachment of the catalytic site to the substrate. Over time, vertically oriented tubes that are attached to loosely bound catalytic sites can be absorbed onto the substrate. In contrast, substrates that had the catalytic sites deposited by molecular beam epitaxy (MBE) have demonstrated reliable pickup of nanotubes with an AFM tip over several years without special care (Hafner J., Rice University, private communications, 2002)

The diameters of the picked-up tubes measured with TEM were typically between 4 and 6 nm. In comparison, the diameters of nanotubes lying horizontally on the

substrate, determined by AFM height measurements, were only 2-3 nm. Deformation of the horizontal nanotube due to van der Waals forces has been modeled using realistic molecular dynamics simulations based on quantum mechanical calculations, and was found insufficient to explain this discrepancy [88]. This indicates that larger diameter tubes are preferentially picked up by silicon AFM probes. One possibility is that larger diameter tubes have a higher probability of remaining vertically oriented on the growth substrate over time than smaller diameter tubes. Because only the tubes that are absorbed to the substrate can be imaged by AFM, AFM images are biaed toward smaller tubes. Alternatively, this disparity may arise from the binding energy of the tube to the AFM tip. The strength of nanotube attachment can be approximated as being linearly proportional to the nanotube diameter using thin-walled cylinder approximation. This increasing binding energy for larger tubes may result in larger diameter tubes being preferentially picked up.

4.2.3 Carbon Nanotube Shortening

A freshly picked-up nanotube typically protrudes from the end of the AFM tip. High-resolution imaging is not possible with such a long nanotube tip due to thermal fluctuations and bending. The nanotube must be shortened before it can be used for imaging. We used a combination of electrical pulse etching [77, 84] and pushing shortening [85].

For the pulse shortening, an HP 8114A pulse generator was hooked up to the Digital Instruments signal access module to generate electric pulses between the tip

and the substrate. Push shortening is performed by incrementally decreasing the tip-sample separation distance during successive force calibrations to push the nanotube up along the side of an AFM tip. This process requires the tubes to be less than 100 nm long, because longer tubes tend to buckle inelastically during this process and cannot be shortened by further pushing. As compared the pulse shortening, the pushing shortening method has very small shortening steps that are fully controllable. So to shorten a nanotube, we first use pulse shortening to shorten the long tube down to $\sim$ 100 nm, and then use push shortening to shorten the tube down to $\sim$ 10 nm.

We obtained similar results for electrical pulse etching with native oxide coated p-silicon, 300 nm thick thermally grown oxide-coated p-doped silicon, and gold-plated silicon substrates. This finding indicates that the entire probe fabrication procedure can be carried out on a single unpatterned, doped-silicon substrate. Thermally grown oxide substrates typically required higher voltages to successfully pulse-shorten than did either native oxide or gold-coated silicon substrate.

4.3 Characterization of SWNT AFM tips

To characterize the effective resolution of the SWNT probes, we imaged nanotubes resting flat on the silicon substrate. We define resolution as the full width of the imaged tube, measured at the noise floor, minus the measured tube height. While nanotubes are convenient samples for determining resolution, they are not infinitely rigid. Dekker's group has shown that the apparent height of a nanotube measured by tapping mode can decrease substantially at high oscillation amplitudes [89]. So, in

the experiments, the oscillation amplitudes was maintained close enough to its freely oscillating value in air to limit this effect to be within 10% of the true nanotube height.

Figure 4.2 shows histograms of the lateral resolutions obtained with SWNT probes fabricated using a growth substrate coated with ferric nitrate catalyst versus those fabricated using ferritin as the catalyst. The variation in nanotube probe performance was greater than we expected based on previous reports. There is a clear shift in the distribution toward higher resolution probes when ferritin was used as the catalyst, consistent with a narrower catalyst size distribution. The wide range in resolution between the two different kinds of substrates as well as from the same substrate was surprising and underscores the importance of specific nanotube characteristics in determining the maximum achievable resolution.

Nearly 100 probes were imaged by TEM to characterize the efficacy of different fabrication techniques. Of these, fourteen SWNT probes imaged by TEM had previously been used for tapping-mode topographic imaging. Figure 4.3 presents a summary of probe characteristics determined by TEM-AFM correlations for the 14 SWNT prones. Entries in bold correspond to probes that demonstrated lateral resolution less than the actual probe diameter.

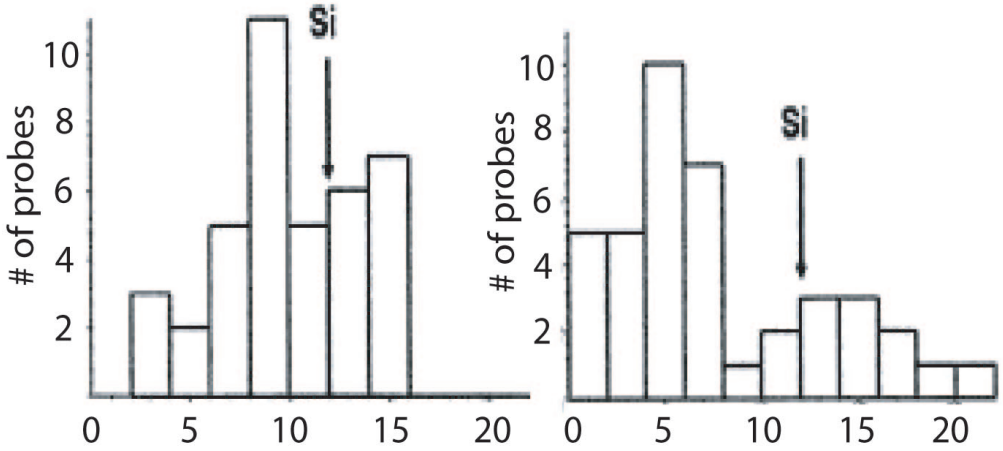

Figure 4.2: The left histogram summarizes the resolution for 39 probes fabricated on a substrate coated with ferric nitrate catalyst. The right histogram shows the resolution distribution of 40 probes made from nanotubes picked up from a substrate coated with ferritin. Included is the typical resolution obtainable with a conventional silicon AFM tip.

Image quality is a function of many factors including: tube diameter and length, contact angle, number of nanotubes extending past the silicon tip, thermal noise, and contamination. These factors can lead to substantial variability in resolution. By correlating probe structure and orientation seen in the TEM images with topographic imaging performance, we can provide experimental evidence consistent with previous mechanical modeling [90], which showed that that lateral tip-sample forces can bend SWNTs or cause snap-to-contact behavior when the tubes exceed either a critical length or a critical angle relative to the substrate surface normal. These effects introduce a significant degree of broadening and appearance of imaging artifacts.

If the nanotube is presented to the sample surface at an angle deviating from the surface normal by more than $\sim 30°$, poor resolution and obvious image artifacts result due to tip-sample forces having a significant component perpendicular to the nanotube

tip type	tube diameter	tube length	aspect ratio	deviation from perpendicular	lateral resolution (full width-height)	lateral resolution/ probe diameter
SWNT	**4.2 nm**	**10 nm**	**2.4**	**10°**	**2.8 nm**	**0.67**
Bundle	**9.3 nm**	**77 nm**	**8.3**	**20°**	**4.0 nm**	**0.43**
SWNT	4.0 nm	112 nm	28	30°	10.4 nm	2.60
SWNT[a]	4.0 nm	19 nm	4.8	40°	4.6 nm	1.15
SWNT	**5.5 nm**	**40 nm**	**7.3**	**20°**	**1.2 nm**	**0.22**
Bundle	**8.0 nm**	**35 nm**	**4.4**	**15°**	**5.6 nm**	**0.70**
SWNT	3.7 nm	30 nm	8.1	30°	5.8 nm	1.56
SWNT[a,b]	4.2 nm	33 nm	7.9	20°	6.0 nm	1.43
SWNT	5.4 nm	38 nm	7.0	10°	5.9 nm	1.09
SWNT	3.5 nm	15 nm	4.3	20°	4.4 nm	1.26
Bundle	5.5 nm	51 nm	9.3	0°	21 nm	4.0
SWNT	**5.3 nm**	**55 nm**	**10.4**	**0°**	**3.9 nm**	**0.74**
SWNT	**6.5 nm**	**42 nm**	**6.5**	**0°**	**4.3 nm**	**0.66**
SWNT	5.4 nm	26 nm	4.8	10°	8.0 nm	1.48

Figure 4.3: TEM-AFM correlation table for single-wall carbon nanotube scannong probes. [a] Probe showed a "shadowing" artifact. [b] Nanotube appeared buckled 16 nm from the end of the tube.

axis. For example, Fig. 4.4 shows a 19 nm long, 4 nm diameter tube projecting from the probe tip at an angle of 40°. This probe produced an image that contained a positive height "shadowing" artifact approximately 10 nm in width parallel to the sample tube. Additionally, the TEM image showed that the nanotube is buckled near the silicon tip. Previous reports have described reversible elastic buckling of the nanotube, which did not have a serious impact on image quality [80, 73, 91]. Our TEM correlations indicate that buckling can be inelastic, resulting in irreversible structural changes. This structural defect results in an effectively lower stiffness for the probe, which we believe is responsible for the decreased resolution and imaging artifacts.

SWNTs must also have aspect ratios less than ~ 10 to be adequate for imaging purposes. Figure 4.5 shows a 4 nm diameter nanotube for protruding 112 nm from the end of the AFM tip, but at an angle deviating from the surface normal by less than 20°.

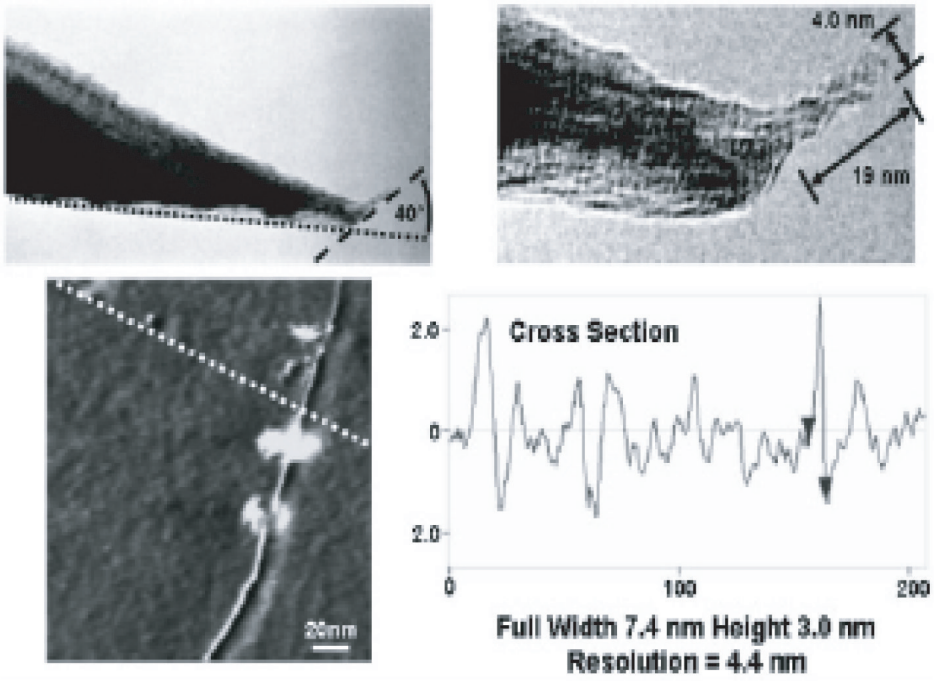

Figure 4.4: Correlation of image showing artifact due to large contact angle with substrate. Additionally, this nanotube appears to be buckled near the silicon tip. The dotted black line in the upper left image is perpendicular to the substrate.

The resulting resolution was still 2.5 times the probe tube diameter. This broadening of the image is in small part due to thermal vibrations. However, mechanical modeling studies have indicated that for a nanotube of this geometry, the root-mean-squared thermal vibrations of the end of the tube should be less than 2 Å [92]. Nanotube bending due to lateral tip-sample forces is most likely the principal contribution to the degraded resolution.

Images taken with high quality nanotube probes show no sign of artifacts. These probes all had the nanotube oriented on the tip at angles close to the substrate surface normal (within 10-20°) and had protrusion lengths $\leq$ 40 nm. By directly measuring the nanotube width from each TEM image and comparing that to the obtained AFM

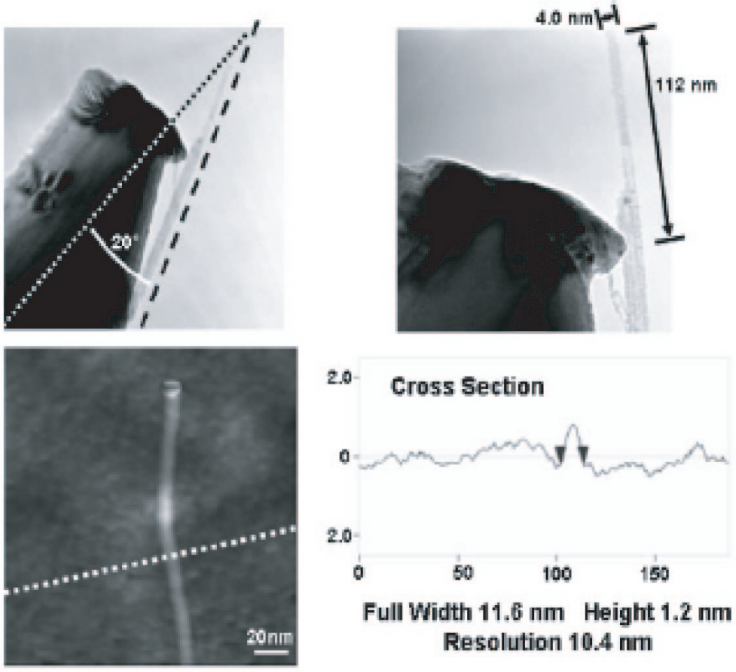

Figure 4.5: Image artifacts due to bending are significant for long nanotubes. Note that there are a number of picked up nanotubes at the base of this tip. The damage to the silicon tip probably occurred during repeated force calibrations.

resolution, we have determined the average ratio of AFM resolution to the tube diameter in this class to be 1.17. This is a reasonable value, given that thermal vibrations and bending will always slightly increase its effective imaging diameter.

In about 1/3 of the high quality nanotube probes made from ferritin substrate, as shown in Fig. 4.6, it was found that the effective lateral resolution was significantly better than the tube diameter measured directly from TEM. Figure 4.6 shows a nanotube probe 5.5 nm in diameter that demonstrated a lateral resolution of 1.2 nm, just 22% of the tube diameter. It is likely that this enhanced resolution occurs when the nanotube contacts the substrate with either an asperity or at a specific angle such that only an edge of the nanotube is in contact with the substrate.

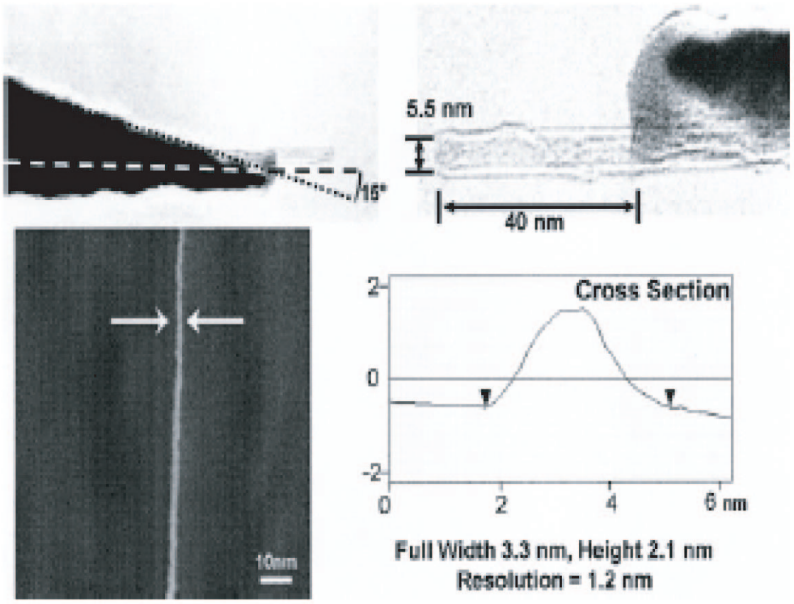

Figure 4.6: TEM-AFM correlation of a SWNT probe that demonstrate an effective lateral resolution that was 22% of the probe diameter.

Chapter 5

Sequence Dependence of DNA Polymerase Incorporation Kinetics

Evidence indicates that kinetics of nucleotide incorporation depends on the DNA sequence context: crystal structures show that the polymerase interact with the DNA bases and DNA sequencing experiments reveal some sequences are more "difficult" to synthesis than others. Although previous measurements have confirmed the dependence of kinetics of nucleotide incorporation on the local sequence, a systematic investigation with DNA sequence permutation has yet to be established. Using microfluidic fast-mixing devices, which demand minimal sample consumption, we made pre-steady state kinetic measurements with local DNA sequence permutation with Klenow exo$^-$. Overall, our results show that k_{pol} is constant across the sequences, while the nucleotide dissociation constant, K_d, varies by ~ 4 fold across the sequences. Comparison of the kinetic results across the sequences indicates that the "open" to "close" conformational change of the fingers subdomain is not rate-limiting and that the transition state of the rate-limiting step does not involve conformational changes that correspond to polymerase-base interaction. With quantitative comparison of

K_d, we show that the binding of the nucleotide to polymerase/DNA is stabilized by base stacking. With the measurements, we are able to give an energetic diagram of nucleotide incorporation for different sequences. We show that systematic kinetic analysis can give insight to the process of DNA synthesis.

5.1 Introduction of DNA Polymerase

DNA polymerases play the central role in DNA replication. Provided with the continual DNA damages and the size of the genome, it is not a simple task to accurately and efficiently replicate the genome. Cells in different organisms have evolved multiple polymerases to meet specific needs of DNA replication [93]. For example, 5 DNA polymerases have been identified in *E. coli*, 8 in *S. cerevisiae*, 12 in *A. thaliana*, and 15 in mammals. The polymerases identified across the species can be classified into seven superfamilies (A, B, C, D, X, Y, RT) based on DNA sequence homology [94, 95].

Despite the lack of common sequence homology, the structures of most DNA polymerases amazingly share a common architecture [96]. Enzymes from different families may contain exonuclease domains and associate with accessory subunits. But in all cases, the polymerase domain is composed of three functionally distinct subdomains, called the fingers, palm, and thumb subdomains. The palm subdomain contains three highly conserved carboxylate catalytic residues that are essential for the phosphoryl transfer reaction; while the fingers subdomain interacts with the incoming nucleotide and the templating base (the base pairing with the incoming nucleotide);

and the thumb helps stabilized the primer-template DNA. All DNA polymerases studied also share a common biochemical pathway [97, 98, 99, 100, 101, 102, 103], regardless of their divergent properties. The basic model of nucleotide incorporation by polymerases is shown in Scheme Ia. The process begins with the binding of the polymerase to the primer-template substrate to form the $D_n{\cdot}E$ complex (S1). The $D_n{\cdot}E$ complex then binds to a nucleoside triphosphate to form the open ternary complex $D_n \cdot E \cdot dNTP$ (S2), a step which is fast and can be considered at equilibrium. The binding of the nucleotide then triggers a conformational change of the fingers domain to close the catalysis cleft to form the closed ternary complex $D_n \cdot E^* \cdot dNTP$ (S3), which is followed by the phosphoryl transfer (S4), another conformational change (S5), and the release of the pyrophosphate PP_i (S6). The enzyme then either translocates on the substrate to start a new round of nucleotide incorporation (indicated in Scheme Ia) or dissociates from the primer-template DNA.

Beyond a common structural architecture and a common pathway of nucleotide incorporation, DNA polymerases exhibit widely divergent properties in terms of fidelity, processivity, primer-template recognition, etc., which are generally in accordance with their specific functional roles in DNA replication (replication initiation, replication, repair, etc.) [104]. Much of the difference is caused by detailed DNA polymerase-substrates interactions, including small differences in the position of critical atoms and in the catalytic electrostatic environment [105]. One fundamental question remained to answer is whether kinetics (rates and dissociation constants) of DNA synthesis depends on the DNA sequence context. Although polymerases inter-

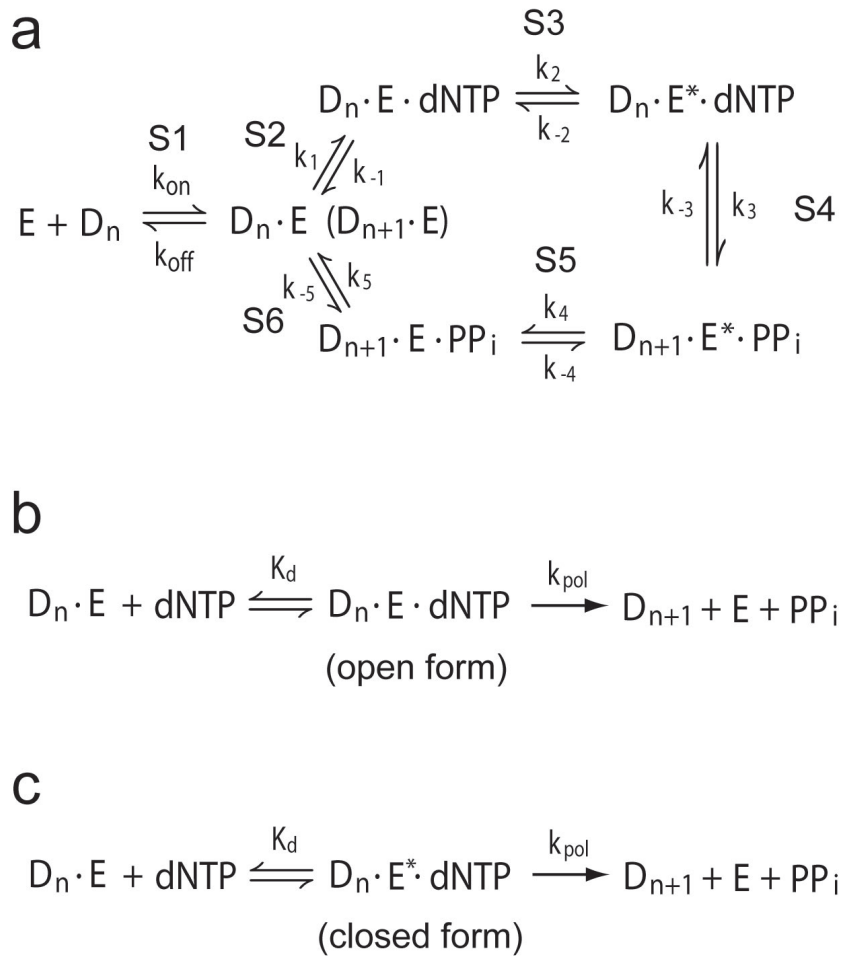

Figure 5.1: The detailed and simplified pathway of nucleotide incorporation.

act mainly with the DNA backbone and the minor groove in a sequence-independent manner [106], crystal structures revealed that polymerases also interact with the nucleobases (Fig. 5.2a), and in the closed ternary complex the last few base pairs at the duplex terminus are changed from B-form to A-form [106, 107, 108, 109]. Early kinetic experiments, many done before the first ternary structure was known, indicated that there is a dependence of incorporation kinetics on the local DNA sequence [97, 98, 110, 111, 112, 113]. The sequence dependence has been observed in kinetics with different polymerases [110, 112, 113], for the incorporation of both correct [111, 112, 113] and incorrect [98, 111, 113] nucleotides, and for DNA-polymerase association [97]. However, variation in rates or constants due to sequence effects is not significant, and is typically within 10 fold [97, 98, 110, 111, 112]. There is no single experiment that has systematically investigated kinetics with sequence permutation, and it is hard to compare results across different experiments to draw a conclusion. To look into how the local DNA sequence may affect nucleotide incorporation, it is thus desirable to make such an investigation with DNA sequence permutation with the same polymerase under the same experimental conditions.

In this paper, we made single-turnover kinetic assays with Klenow exo$^-$ with DNA sequence permutation at the duplex terminus and the template base $5'$ to the templating base. We employed a fast mixing microfluidic device (Fig. 5.3a) to carry out the assays. The device has mixing time of four milliseconds and uses reagents at only $\sim$ nl (10^{-9})/s, which allows us to make pre-steady state measurements with very small reagent consumption. We show that by making careful kinetic measurements

with DNA sequence permutation, one can shed light into the details of nucleotide incorporation.

5.2 Experimental Procedures

5.2.1 Fast-Mixing Chips

Kinetic measurements were carried in novel microfluidic fast-mixing devices (Fig. 5.3a). The devices dispense reagents into micro "water-in-oil" droplets, where mixing takes place. To fabricate a device, we first made the pattern piece using soft-lithography technology[114]. Briefly, we designed the 2-D channel pattern using a CAD program and printed the pattern on a transparency film (at 40k dpi resolution, by FineLine Imaging, CO); we used the transparency as a photomask for photolithography and made a master mold; we cast mixture of 5:1 (A:B) polydimethylsiloxane (PDMS) monomers (General Electric) on the mold, let the monomers crosslink in an $80°C$ oven for 1 hour, and then peeled the PDMS replica off the master mold. PDMS polymer is optically clear and generally inert. The channels are 10 μm in width and in height. We then bonded this PDMS replica to a glass slide that was coated with a thin layer of PDMS film ($\sim$ 20 μm). To ensure strong bonding between the PDMS replica and the PDMS layer, we baked all the devices in an $80°C$ oven for over 72 hours.

Fluid flows in the channels were driven by pneumatic pressures applied at the liquid inlet ports. After baking, the devices can sustain pneumatic pressures up to

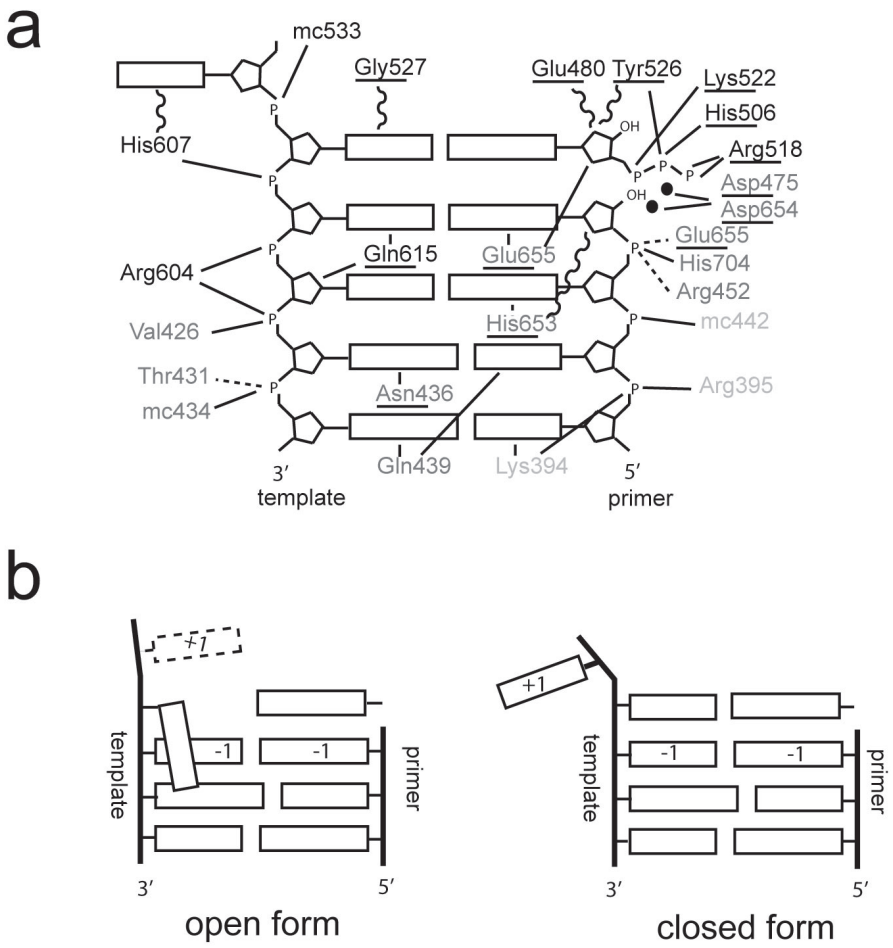

Figure 5.2: Schematic illustration of polymerase-DNA/nucleotide interaction and DNA conformation. **a**. Polymerase contact with the primer template and the nucleotide according to Doublié et al. [106]. Polymerase residues are in close contact to the DNA backbone, bases, and the nucleotide with direct (solid lines), water-mediated (dotted lines) and van der Waals (wavy lines) interactions. The interactions distort the double-stranded DNA, bending and compressing it. Right after the active site, the single-stranded template undergoes a sharp kink due to the strong interactions between residue Gly527 and the template base, and between residue His607 and the +1 base. Residues that are conserved of the Pol I family are underlined, and all the residues are color-coded for the finger (black), palm (dark grey), and thumb (light grey) subdomains. **b**. Illustration of the conformation of DNA at the open ternary form and closed ternary form. In the open form, the +1 base is disordered in crystal structure and the templating base lies on the side of the duplex contacting the -1 base on the template. In the closed form, the templating base is back at the position base-pairing with the nucleotide, while the +1 base is flipped out with a kink at the backbone.

30 psi. The volume of the droplet solely depends on the flow rate ratio of aqueous liquid and the oil and can be tuned from 0.8 to 4 picoliter (see Chapter 6). To precisely control the flow rates and thus the droplet volume, we used electro-pneumatic transducers with ± 0.03 psi accuracy (Type 2000, Marsh-Bellofram) to regulate the pneumatic pressure at the liquid inlets. The flow rate in the reaction channel typically ranges from 2 nl/s to 5 nl/s, depending on the pressure applied. The small material consumption gives a major advantage to the microfluidic devices.

As the droplets go through a serpentine channel, the aqueous solution inside the droplet circulates, which promotes mixing. We calibrated the mixing time of our devices by mixing Cy3-dCTP and Buffer 2. Our measurement of Cy3 fluorescence at the buffer side showed the fluorescence reached the maximum in 4 milliseconds (Fig. 5.3b), indicating the mixing was complete. Mixing time of a couple of milliseconds was demonstrated previously with similar devices[115, 116]. Klenow incorporates nucleotides on the time scale of tens of millisecond; so the mixing time of four milliseconds fast enough for making pre-steady kinetic measurement.

5.2.2 Materials

Klenow exo$^-$ is the fragment of *E. coli* Pol I with the removal of both the 5′ nuclease domain and the 3′ exonuclease domain. *E. coli* Pol I was the first DNA polymerase discovered and isolated, and has been relatively well studied as one of the model polymerases. We used Klenow exo$^-$ in our experiments. The Klenow exo$^-$ enzyme was purchased from New England Biolabs. Cy3 labeled dCTP was purchased from GE

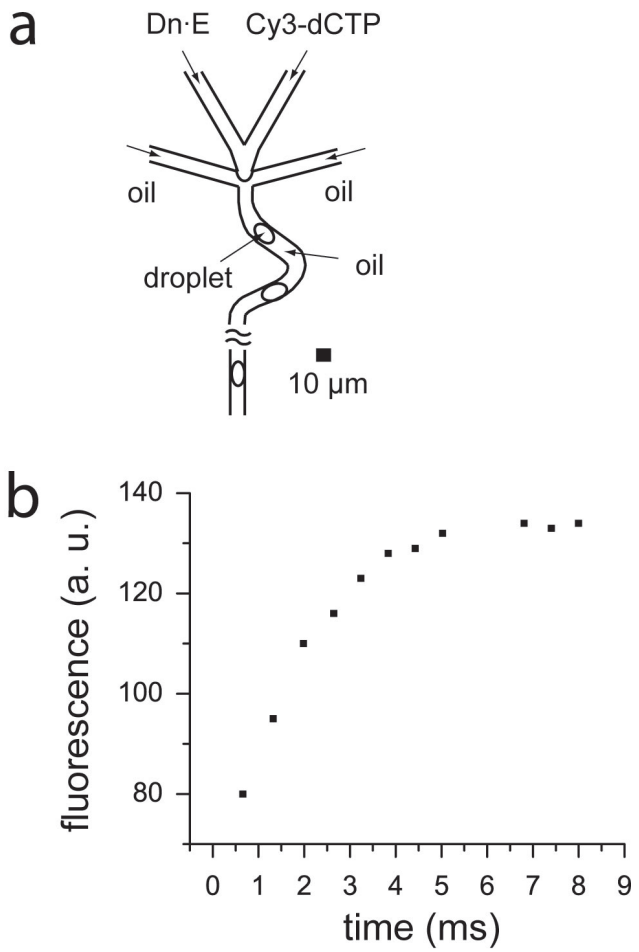

Figure 5.3: The fast-mixing microfluidic chip for kinetic measurements. **a**. A diagram of the chip. **b**. Calibration of the mixing time. For calibration, we put Cy3-dCTP (1 μM) and Buffer 2 in the two center channels. The data shows the Cy3 fluorescence measured along the reaction channel.

Health Care (Amersham, UK) at the concentration of 100 mM. The DNA oligonucleotides, the templates and primers, were custom synthesized by IDT (Coralville, IA). The primers are a 22-mer (5′ TGCTGGGCTTTTGGTTTGTGGX), and is internally labeled with Alexa Fluor 647 dye (Molecular Probes) at the -8 base (indicated in italic). The templates are a 41-mer (3′ acgacccgaaaaccaaacaccxgycatacaagaagccatcc), with the template base (against which the incoming nucleotide is added) indicated in bold. We used the capital and lower case letters for the primer and template bases, respectively. The bases underscored, X and x at the -1 position, and y at the +1 position, were permutated (Scheme II). Because we were interested in kinetics of single base incorporation, we avoided processive incorporation of dCTP by varying the +1 base only among c, a, and t. In total, we had 12 (4×3) primer-template sequences.

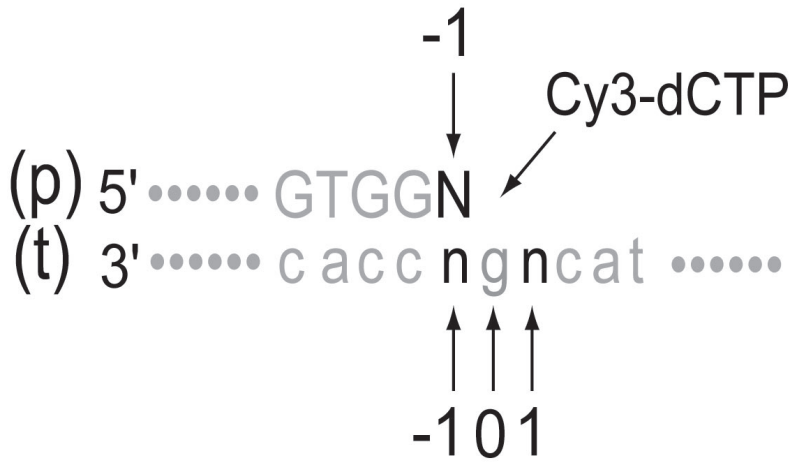

Figure 5.4: DNA sequence permutation at the -1 and +1 position.

For the oil, we used equal-volume mixture of fluid EGC-1702 (3M), Fluorinert 72

(3M) and Fluorinert 84 (3M). Fluorinert is the trademark name of 3M for perfluorocarbon compounds which replace hydrogen atoms by fluorine atoms, and EGC-1702 is a hydrofluoroether solvent. These fluids are inert, with perfluorocarbon being commonly used in eye surgery and as artificial blood in emergency. To lower the surface energy of droplets, we added 10 % v/v 1H,1H,2H,2H-perfluoro-1-octanol (Sigma-Aldrich) as surfactant in the oil mixture. This highly perfluorinated surfactant is not soluble in water, so any extra surfactant stays in the oil.

5.2.3 Pre-steady State Kinetic Measurements

All DNA synthesis experiments were carried out at $21°C$ in 10 mM Tris-HCl, 50 mM NaCl, 10 mM $MgCl_2$, 1 mM Dithiothreitol (Buffer 2, New England Biolabs) and 10 mM $MnCl_2$. The primer-template oligonucleotides and the polymerase were pre-incubated (at 1:2 oligo:enzyme molar ratio) to form $D_n \cdot E$ complex. The $D_n \cdot E$ complex and the Cy3-labeled nucleotides (at 10× concentration of the oligonucleotides) were delivered from the two aqueous channels to form "water-in-oil" droplets (Fig. 5.3a). Fluorescence resonance energy transfer (FRET) along the reaction channel was detected with a Nikon microscope with a mercury lamp, a 20× objective, a Cy3/Cy5 excitation/emission filter set (Chroma Technology), and a $-80°C$ CCD camera (Cascade II, Photometrics). The time course of a reaction was obtained by measuring by converting the position along the reaction channel to reaction time. To optimize the signal-to-noise ratio, each data point was averaged along a segment of $\sim 50\ \mu m$long. To exclude artifacts due to non-uniform fluorescence in the field of view, we recorded

one image for each data point and took the fluorescence signal from the same subblock in the field of view.

5.3 Results

5.3.1 Kinetic Measurements

For Klenow, the dissociation rate of $D_n \cdot E$ ($k_{off} \sim$ 0.01-1 s^{-1})[97] is much slower than the nucleotide incorporation rate. In single-turnover assays, step S1 can be avoided with pre-incubation of the primer-template DNA and the enzyme. The simplified pathway is shown in Scheme Ib and Ic. The nucleotides first bind to $D_n \cdot E$ with an apparent dissociation constant Kd to form the intermediate specie, $(D_n \cdot E \cdot dNTP)_{int}$. $(D_n \cdot E \cdot dNTP)_{int}$ can be either the open form $D_n \cdot E \cdot dCTP$ if step S3 is rate-limiting (Scheme Ib) or the closed form complex $D_n \cdot E^* \cdot dCTP$ if step S3 is not rate-limiting and is fast compared to mixing (Scheme Ic). The next step in the simplified pathway has a rate of k_{pol}, which is determined by the rate-limiting step among S3-S6 or S4-S6, depending on which form $(D_n \cdot E \cdot dNTP)_{int}$ takes.

Nucleotide incorporation was detected by fluorescence resonance energy transfer (FRET) between Cy3 (donor) on the nucleotide and Alexa Fluor 647 (acceptor) at the -8 position of the primer. The FRET signal is proportional to the sum of $[D_{n+1}]$ and $[(D_n \cdot E \cdot dCTP)_{int}]$. Since the nucleotide was at 10× concentration of the DNA substrate, [dCTP] can be considered as constant. With simple algebra, the sum of

$[D_{n+1}]$ and $[(D_n \cdot E \cdot dCTP)_{int}]$ can be written as

$$[D_{n+1}] + [(D_n \cdot E \cdot dCTP)_{int}] = c_1 - c_2 exp(-k_{obs}t), \tag{5.1}$$

where

$$k_{obs} = k_{pol} \frac{[dCTP]}{[dCTP] + K_d}. \tag{5.2}$$

The two constants c_1 and c_2 depend on the fluorescence background, the nucleotide concentration, and the setting of the camera of a specific assay. For each assay at a specific nucleotide concentration, we fitted the time course of the FRET signal to Eq. (5.1) to obtain the apparent rate of nucleotide incorporation, k_{obs} (Fig. 5.5a). We then fitted k_{obs} obtained with different nucleotide concentrations to Eq. (5.2) to obtain k_{pol} and K_d (Fig. 5.5b).

5.3.2 The Rate-Limiting Step

We measured k_{pol} and K_d for 12 different DNA substrates. Our result of k_{pol} ($\sim$ 30 s^{-1}) (Fig. 5.6a) is about one fold smaller than previous measurements with natural nucleotides [97, 117]. It is intriguing that k_{pol}, which is the rate for the rate-limiting step, is constant across sequences (Fig. 5.6a). Base on the observation of small α-phosphothioate elemental effect [97, 118]and crystal structures [107, 109], it was widely thought that the "open" to "close" conformational change step (step S3) is rate-limiting. Crystal structures show significant difference in DNA conformation between the closed form and the open form ternary structures [109]. In the open ternary

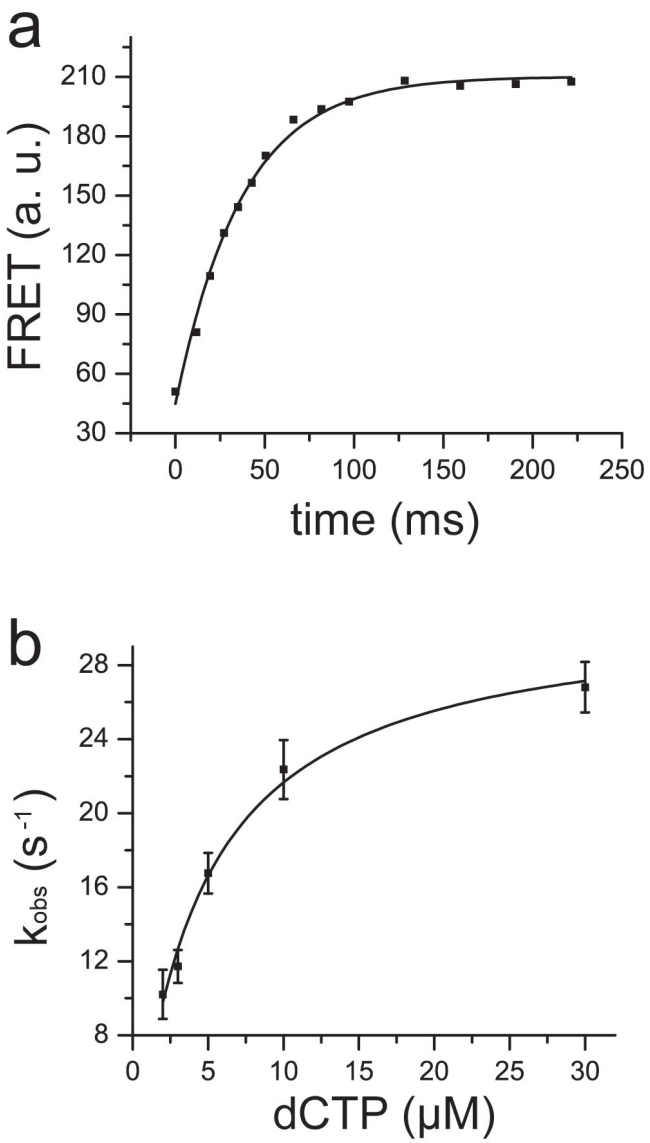

Figure 5.5: Pre-steady kinetic measurements. **a**. The time course of fluorescence resonance energy transfer (FRET) signal (filled squares) is fitted to Eq. (5.1) (curve), which gives the apparent rate of nucleotide incorporation, k_{obs}, at the specific nucleotide concentration. **b**. The data of k_{obs} (filled squares) at different dCTP concentration are fitted to Eq. (5.2) (curve), which gives the maximum rate of nucleotide incorporation k_{pol}, and dissociation constant of the nucleotide K_d. The data shown in this figure are for sequence (3′)ggc (in the order of -1 0 1 for the template)

structure, the +1 base is disordered, and the templating base is displaced from the base-paring position to lie on the side of the DNA duplex, where it is stabilized by contacting the previous template bases (Fig. 5.2b). It follows that the free energy of the open form varies for different -1 and +1 template bases. In the closed ternary structure, the templating base is at the base-paring position, and the template strand undoes a sharp kink on the 5′-phosphodiester linkage to the templating base, such that the +1 template base is flipped out of the stacking arrangement with the DNA duplex. Polymerases of different families including Pol I [107, 119] were shown to have the kink feature, which allows a residue in the fingers subdomain to stack on the template base to impose a geometry check for correct Watson-Crick base paring, and protects DNA synthesis from frame shifting. The transition from the open form to the closed form disrupts the contact between the templating base and the -1 base on the side, and stabilizes the +1 base. It is anticipated that the rate of the open to closed form transition (step S3) depends on the -1 and +1 bases. The fact that k_{pol} does not depend on the sequence indicates that this step is not rate-limiting.

Our measurements of K_d range from 1 μM to over 4 μM (Fig. 5.8a). Specifically, K_d shows little dependence on the +1 base. This independence is expected because in the closed form, the +1 base on the template is flipped out of the stacking arrangement with the DNA duplex, such that it makes sense little contact with the duplex terminus and should not affect K_d.

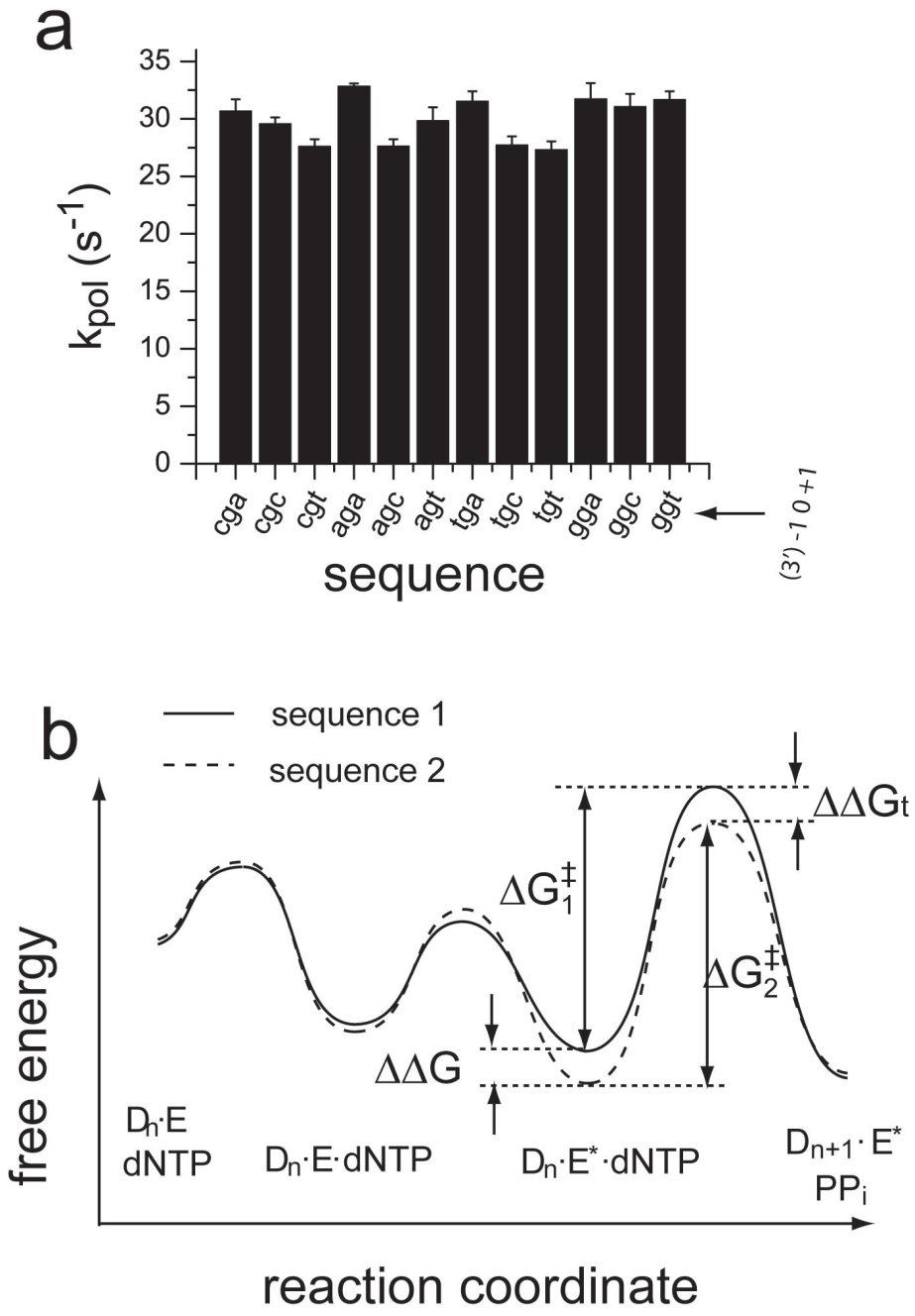

Figure 5.6: The maximum rate of nucleotide incorporation, k_{pol}, across the sequences. **a**. k_{pol} shows no apparent dependence on the DNA sequence. The sequences shown on the axis are for the template, as marked on the right side of the horizontal axis. **b**. Schematic illustration of the free energy along the reaction coordinate. The dash curve and the solid curve represent two different sequences. Constant k_{pol} indicates that the activation energy $\triangle G^{\ddagger}$ for the two sequences is the same, or the free energy difference ($\triangle\triangle G$) of the closed form complexes is the same as the free energy difference ($\triangle\triangle G_t$) of the transition states.

5.3.3 Base Stacking

The dissociation constant K_d shows ~ 4 fold variation across different base pairs at the -1 position (Fig. 5.8a). The table lists K_d (averaged among different +1 bases) for different -1 base pairs. Generally, K_d should depend on the ground state free energy of $D_n \cdot E^* \cdot dNTP$ (Fig. 5.6b), which can be stabilized by hydrogen bonding between the nucleotide and the templating base, interaction between the polymerase and the DNA/nucleotide, and base stacking between the nucleotide and the $3'$ primer end. It is not clear which of these interactions are actually involved or important in stabilizing the ternary complex, although some experiments on non-Watson-Crick base incorporation showed that higher base stacking energy facilitates nucleotide insertion. By measuring K_d for different sequences, we can quantitatively compare the ground state free energy and the base-stacking free energy for two sequences. We calculated the free energy difference of the $D_n \cdot E \cdot dNTP$ complexes for two sequences ($\triangle\triangle G = \triangle G_{seq2} - \triangle G_{seq1}$) according to thermodynamics,

$$\triangle\triangle G = RTln(K_{d,seq2}/K_{d,seq1}), \tag{5.3}$$

and calculated the base-stacking free difference between the nucleotide and two different $3'$-end primer bases, $\triangle\triangle G^{stk} = \triangle\triangle G^{stk}_{seq2} - \triangle\triangle G^{stk}_{seq1}$ (Table). $\triangle\triangle G$ and $\triangle\triangle G^{stk}$ agree well between duplex terminus (primer/template) G/c and C/g or between A/t and T/a (Fig. 5.85b), indicating that base stacking stabilizes the nucleotide.

primer 3'-end	K_d (μM)	ΔG^{stk} (kcal/mol) stacking energy between C and primer 3'-end base
G	2.26 ± 0.23	-4.06
C	4.21 ± 0.43	-3.58
A	1.18 ± 0.16	-3.72
T	1.11 ± 0.15	-3.85

Figure 5.7: The nucleotide dissociation constant (K_d) and base-stacking free energy ($\triangle\triangle G^{stk}$) with different -1 primer bases. Since K_d does not depend on the +1 base, each listed value is the average of different +1 bases. The base-stacking free energy is according to Friedman at al.[120].

5.3.4 The Transition State

That k_{pol} is approximately constant indicates that the activation energy $\triangle G^{\ddagger}$ for different sequences is the same (Fig. 5.6b). It follows that between two sequences, the free energy difference of the closed forms, $\triangle\triangle G$, is the same as the free energy difference of transition state, $\triangle\triangle G_t$. The same amount of free energy shift in ground state and TS implies there is little change in the polymerase-DNA base interaction from the close form to the TS II. However, there may be conformational changes involving atoms on the primer backbone terminus or the nucleotide triphosphate, since such changes would not affect two sequences differentially.

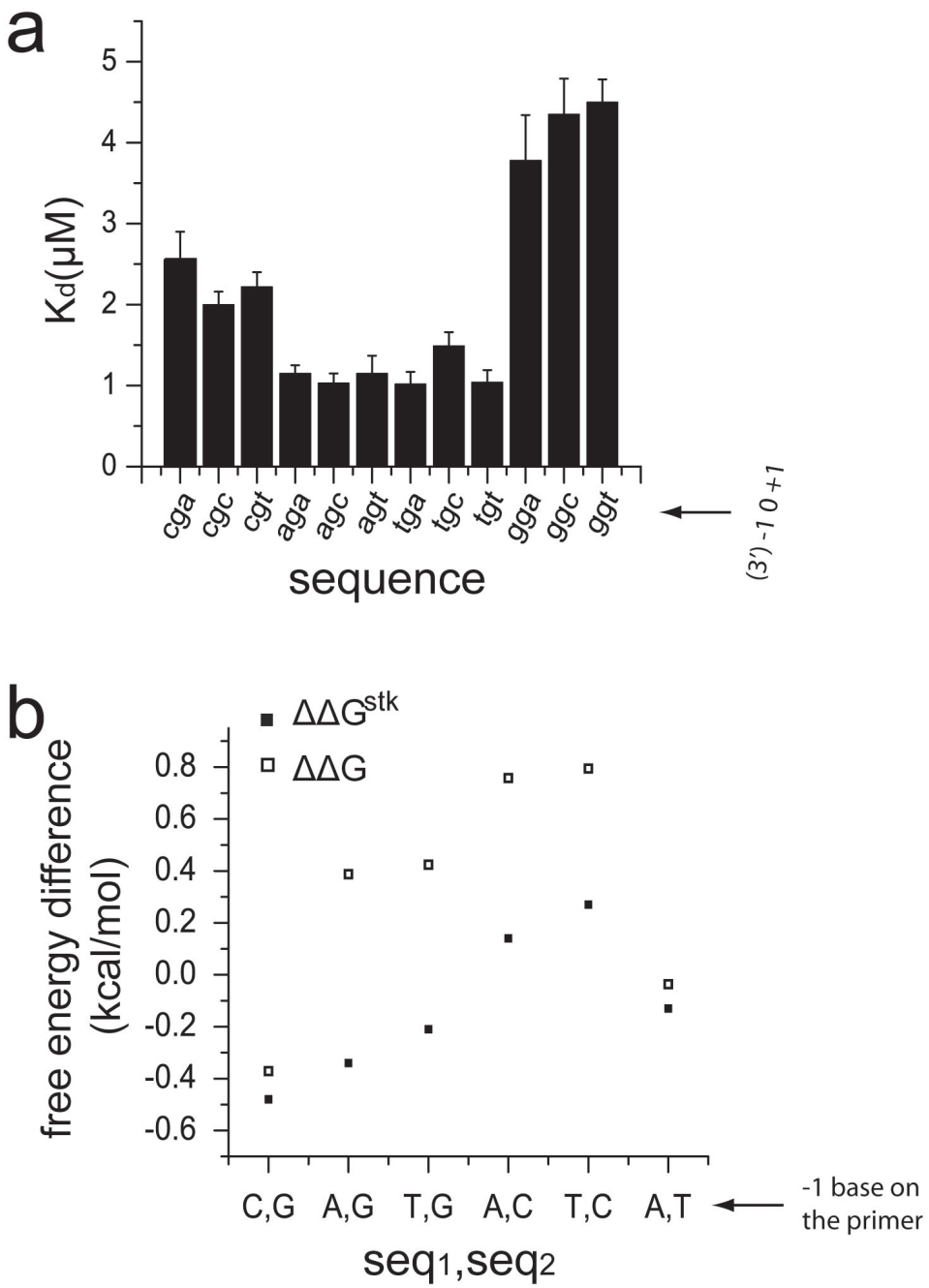

Figure 5.8: The dissociation constant of the nucleotide, K_d, across the sequences. **a**. K_d does not show evident dependence on the +1 base, but show a variation more than 4 fold correlating with the -1 base pair. The sequences shown on the axis are for the template, as marked on the right side of the horizontal axis. **b**. Comparison between $\triangle\triangle G$ and $\triangle\triangle G^{stk}$ for two sequences. $\triangle\triangle G$ is the free energy difference of two closed ternary complexes with different DNA sequences, and is calculated according to Eq. (5.3). $\triangle\triangle G^{stk}$ is the free energy difference of base stacking between the nucleotide and two different primer terminus bases, and is calculated as $\triangle\triangle G^{stk} = \triangle\triangle G^{stk}_{seq2} - \triangle\triangle G^{stk}_{seq1}$.

5.3.5 Energetics of Nucleotide Incorporation

To summarize our findings from the kinetic results, we draw a schematic diagram of the energetics of nucleotide incorporation with different +1 bases (Fig. 5.9a) and with different -1 base pairs (Fig. 5.9b). We purposely draw the free energy of the binary complex of different sequences at the same level to emphasize the energetic difference among the sequences along the reaction coordination. For the closed form as well as the TS II, the free energy difference between sequences can be inferred from Eq. (5.3). However, there is not much information on the free energy difference between sequences for the open form and the TS I (marked by $*$), and the energy levels were drawn only for the purpose of illustration.

5.4 Discussion

Indeed, that the "open" to "close" conformational change step is not rate-limiting has been suggested by studies of site-directed mutagenesis for pol β [121, 122, 123, 124], and recent direct measurements with FRET showed that this step is very fast for Klentaq [125] and T7 pol [126]. A study by Bakhtina et al. using 2-aminopurine fluorescence suggests that a fast conformational change step might exist for both the X family and Pol I [127]. Our measurements support the conclusion from an orthogonal approach. With the "open" to "close" conformational change step being fast, the polymerase/DNA/nucleotide complex at equilibrium should be mostly in the closed form (Scheme Ic). This is important to note because it was often assumed that the complex after mixing is in the open form (Scheme Ib), partly because step

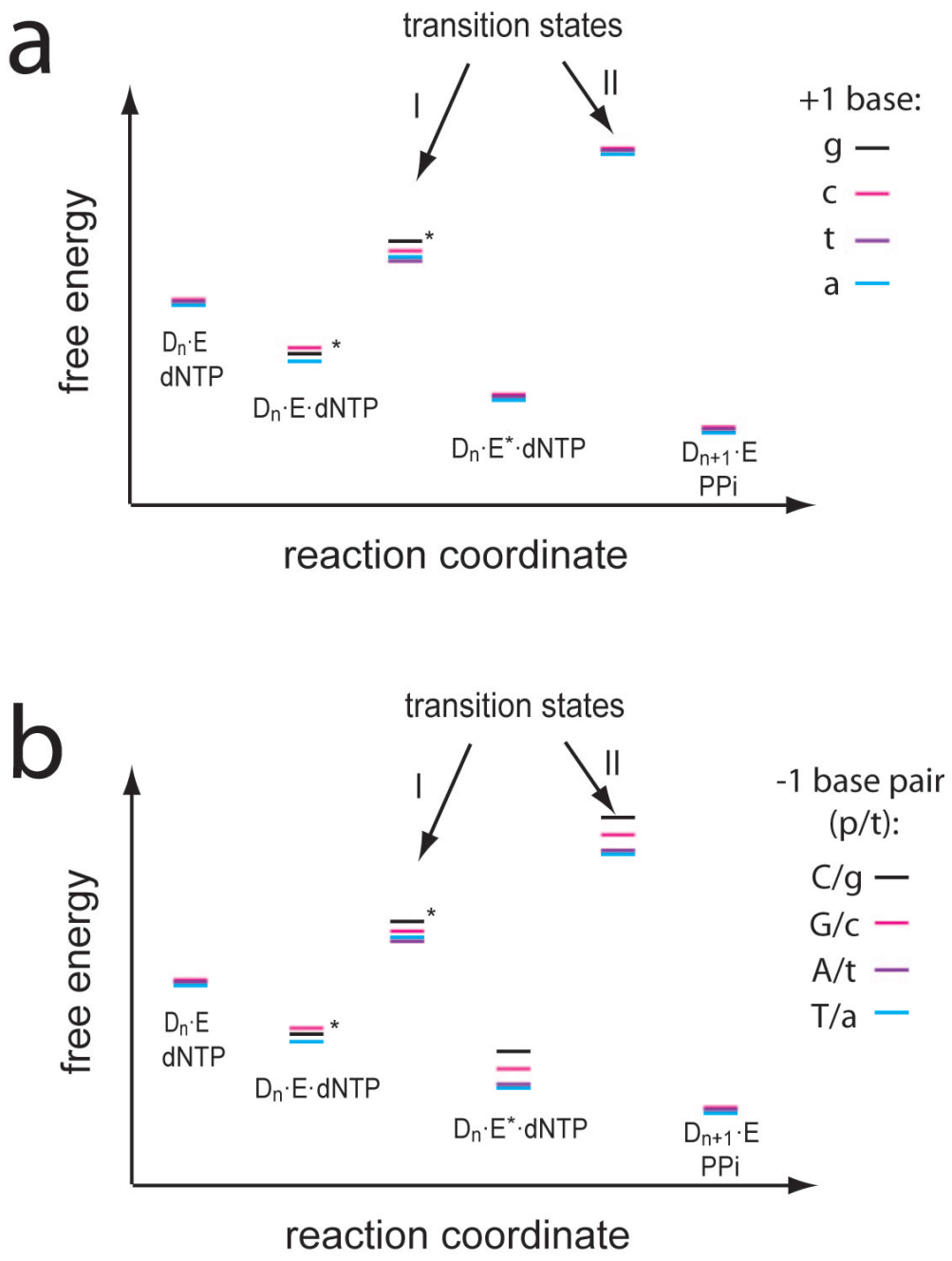

Figure 5.9: Energetics of nucleotide incorporation for different sequences. Note that for the open form and the TS I (marked by $*$), the free energy difference between sequences is not certain and sketch in the figure is only for illustration. We also ignore the difference in the free energy of the binary complexes for different sequences, and sketch the binary complexes at the same level to emphasize the energetic change among the sequences along the reaction coordination. **a**. Energetics of nucleotide incorporation for sequences with different bases at the +1 position. The free energy for the closed and the TS II is the same for different +1 bases (see the text). **b**. Energetics of nucleotide incorporation for sequences with different base pairs at the -1 position. For the closed form, the difference of the free energy difference between sequences can be calculated from Eq. (5.3). As discussed in the text, TS II has the same free energy differences between sequences as the closed form.

3 was previously believed as rate-limiting.

It was pointed out [105] that the components at the catalytic site, including the C3′ atom on the primer terminus, the αP of the incoming nucleotide, the two Mg^{2+} metal ions, and the catalytic residues must be properly coordinated before the nucleotidyl transfer can happen. With the structure of a pol β ternary complex that has intact primer 3′-OH and two Mg^{2+} ions[128] as the initial state, theoretical calculations yielded TS that is distinct from the initial crystal structure, which is supposed to be the ground state of the closed form, and the calculated activation barrier agrees with the experimentally measured activation free energy [**?**]. The agreement suggests that the process of nucleotidyl transfer post the closed ternary form is the rate-limiting step.

It has been previously suggested that base stacking stabilizes nucleotide binding. It was found that DNA polymerases can add a nucleotide against an abasic site or create a dangling base at the 3′ primer end with preference for pyrimidines which have higher stacking energy [129, 130]; it was shown that nucleotides analogs with strong base stacking energy were inserted much more efficiently than natural ones [131]. Our experiments showed that $\triangle\triangle G$ and $\triangle\triangle G^{stk}$ do not agree for all sequences, but the quantitative agreement between C/g and G/c, and between A/t and T/a, indicates that base stacking is important for nucleotide stabilization.

Figure 5.8 shows that $\triangle\triangle G$ and $\triangle\triangle G^{stk}$ differ by ~ 0.6 kcal/mol between A/t and G/c, T/a and G/c, A/t and C/g, and T/a and C/g. Apparently, interactions other than base stacking are involved in stabilizing the complex. Noticeably, the dif-

ference of $\triangle\triangle G$ and $\triangle\triangle G^{stk}$ is observed between A/t, T/a and G/c, C/g. Although the A/t (or T/a) base pair and the G/c (or C/g) base pair have different hydrogen bonding strength, the same amount of difference should be in the binary ground states and should not cause difference in K_d between the two groups. But if in the ternary complex the DNA conformation is changed during nucleotide incorporation, which requires a larger amount of free energy penalty for G/c (C/g) because it is more stable than A/t (T/a), it is possible that the ternary complex with G/c (C/g) as the -1 base pair is less stable and has higher K_d. Without the energetics of the nucleotide binding process, a quantitative examination is lacked.

Although crystal structures show that the polymerase residues interact strongly with the DNA backbone and bases, subtle conformational changes that correspond to a few fractions of hydrogen bonding are often difficult to capture, even with high-resolution crystallography. Arrehnius equation ($k = k_0 exp(-\triangle\triangle G/RT)$) states that a small change in the free energy can shift the rate or equilibrium significantly; for example, 1.3 kcal/mol of $\triangle\triangle G$ corresponds to one order of magnitude change in the rate or equilibrium constant, and 0.4 kcal/mol to two fold of change. By making kinetic assays with DNA sequence permutation, we can shed light onto the important polymerase-DNA interactions that are not available from crystallography.

In our experiments we used fluorophore-labeled nucleotides. The results are relevant to the increasing number of applications where labeled nucleotides are used. Example applications include polymerase chain reaction (PCR) and the new generation of fast DNA sequencing techniques (sequencing by synthesis). For these ap-

plications, the properties of DNA polymerases have a pivotal role [132, 133], and a knowledge of the enzyme is essential for technology development. However, it is not clear how the fluorescent labeling (Cy3, in this case) may interfere with the polymerase-DNA/nucleotide interaction and whether the current results are applicable to natural nucleotides. Nevertheless, our results agree with recent studies of the rate-limiting step that used either labeled or natural nucleotides, and are in line with crystal structures and previous studies that suggested the role of base stacking in stabilizing nucleotide binding. By providing insights to polymerase-DNA/nucleotide interactions, our results should help the understanding of the process of nucleotide incorporation.

Chapter 6

Mechanism of Droplet Formation in Microfluidic Channels

6.1 Introduction

Droplets, simple patterns of one liquid phase dispersed in another, are fundamentally important in nature and in technology. The physical process of pattern formation is associated with elements of nonlinearity and instability [134], and a complete characterization requires large-scale numerical simulation with detailed knowledge of boundary conditions. On the other hand, valuable understanding can be gained from asymptotic models applying for limiting cases. At small length scales, the Navier-Stokes equation becomes linear, and instability due to inertia does not exist. It has been demonstrated that microfluidic devices can be used to create rich patterns and highly monodispered droplets [135, 136, 137, 138]. As microfluidics grows to become a full-fledged technology, there is also a growing motivation to exploit droplets generated and tailored in microchips, with applications made including fast mixing [115, 116, 139], protein crystallization [140, 141, 142], material fabrication [143], storage [144], and mostly recently, fluidic logic circuits [145, 146, 147]. Chip-

based droplets also poise attractive for applications such as high-throughput assay (e. g., digital-PCR), optofluidics, and trapping. The full advantage of this technology, though, can not be taken until the exact mechanism of droplet formation is clear,

We demonstrated that droplet breakup is a quasiequilibrium process. We found that the volume of the droplets is strictly linear to the ratio of the aqueous flow rate Q_d to the oil flow rate Q_c, with the proportionality constant in agreement with numerical calculation. The absolute flow rate or the viscosity of the fluid does not change the linear relationship, but the geometry of the microchannels does. The process of droplet formation is highly reproducible, and the sizes of droplets can be precisely controlled by tuning the flow rate ratio of the two liquid phases, which allows the formation of highly monodispersed, customer-tailored droplets in microchips.

6.2 Mechanism of Droplet Formation

6.2.1 Previous Results

Droplet formation in a steady flow was first considered by Taylor [148], whose work was later followed and confirmed by others. Taylor predicted that droplet breakup should occur when the viscous stresses that deform the droplet overcome the surface tension stresses that resist the deformation. Balancing the viscous stresses $\eta\dot{\gamma}$ (η: shear viscosity; $\dot{\gamma}$: the shear rate) with the surface tension stresses σ/R (σ: interfacial

tension; R: radius of the droplet) correctly scales the droplet size as [135, 149, 150]

$$\frac{R}{w} \sim \frac{\sigma}{\eta u}, \tag{6.1}$$

where $\eta u/\sigma$ is defined as Capillary number, C_a, u is velocity of the fluid, and w is width of the channel. However, typical liquid flows in microfluidic channels ($\eta \approx 1mPa \cdot sec$, $\sigma \approx 10mN/m$, and $u \approx 10^{-3} - 10^{-1}m/sec$) have a very small Capillary number ($C_a \approx 10^{-4} - 10^{-2}$), and Eq.(6.1) does not hold because surface tension overwhelms over viscosity. In this case, previous studies show that the droplet size depends on parameters including Capillary number C_a [151], flow rate of the continuous phase Q_c [137], the dispersed phase Q_d [139], or both of them [150, 152]; these measurements unfortunately failed to yield physical models to illustrate the underlying mechanism. Interestingly, Garstecki et al. [153] fit the droplet size to $1 + \alpha Q_d/Q_c$, but the results did not attain the precision to allow a rigorous check; another experiment failed to fit to this formula [152], and it seems that chip geometry also plays a factor in droplet formation. So far, previous experimental studies have not allowed an unambiguous determination of the exact mechanism of droplet formation.

6.2.2 The Linear Relationship

To form droplets, two immiscible liquid phases are typically brought to merge at a T-junction of microchannels [135], where one liquid phase is forced to disperse in the other. Although the T-junction is widely adopted, it is also possible to arrange the channels in a concentric matter, such that the dispersed phase is flow focused by the

continuous phase [138, 154], (Fig. 6.1a). The advantage of such symmetric geometry is that the process of droplet formation evolves symmetrically and is convenient for analysis. In our experiments, we adopted such symmetric arrangement of channels, which have a cross-section of $10\mu m \times 10\mu m$ (Fig. 6.1a). The length and volume presented in this paper is normalized according to the length scale, $w = 10\mu m$; that is, length is normalized by w, and volume is normalized by w^3.

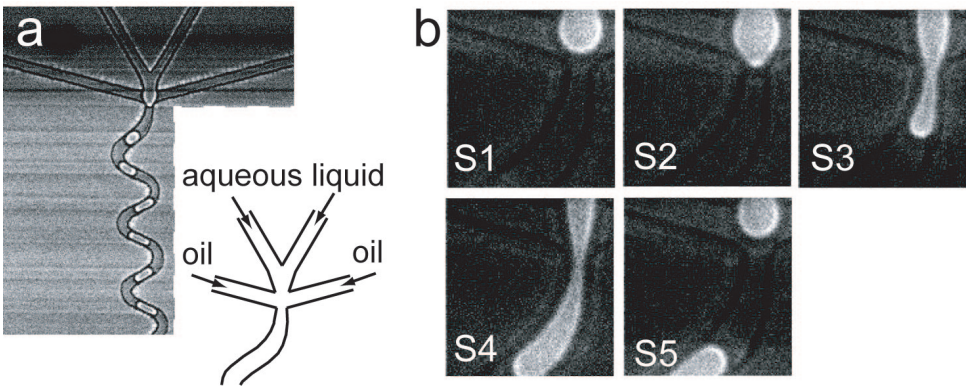

Figure 6.1: Bright-field images of droplet formation in a symmetric microfluidic chip. (a) Droplet formation in the chip where the channels are arranged symmetrically. All the four incoming channels and the common channel are 5 mm in length and 10 μm in width and height. The inset shows a detailed diagram of the junction of the channels. (b) Images capture the five representative stages of droplet formation: growth (S1), blocking (S2), squeezing (S3), breakup (S4), and relaxation (S5). These images were selected from a sequence of images taken at a frame rate of 17 Hz, with exposure time of 10 μsec.

Figure 6.1b shows typical images of a cycle of droplet formation. First the tip of the aqueous stream grows, then it enters and blocks the downstream channel; the oil starts to squeeze the aqueous stream, forming a pinch on it; the tip of the aqueous stream continues to grow until it breaks apart from the stream. This process is highly stable, being repeated from cycle to cycle. It is understood that a jet of fluid with free

surface can undergo breakup simply because of surface instability: any axisymmetrical perturbation with wavelengths longer than the perimeter of the jet can reduce the surface area and lower the surface energy, so the perturbation grows and leads to the breakup of the jet (Fig. 6.2a). This is called Rayleigh-Plateau instability, and is exactly the mechanism for the breakup of water jets emerging from kitchen taps. However, in our system, surface instability initially cannot grow because the aqueous stream is confined by the channels except at the junction which is shorter than the perimeter of the thread. The highly monodispersed droplets formed are manifest of the lack of Rayleigh-Plateau instability in the first stage because droplets formed by surface instability are highly polydispersed in size.

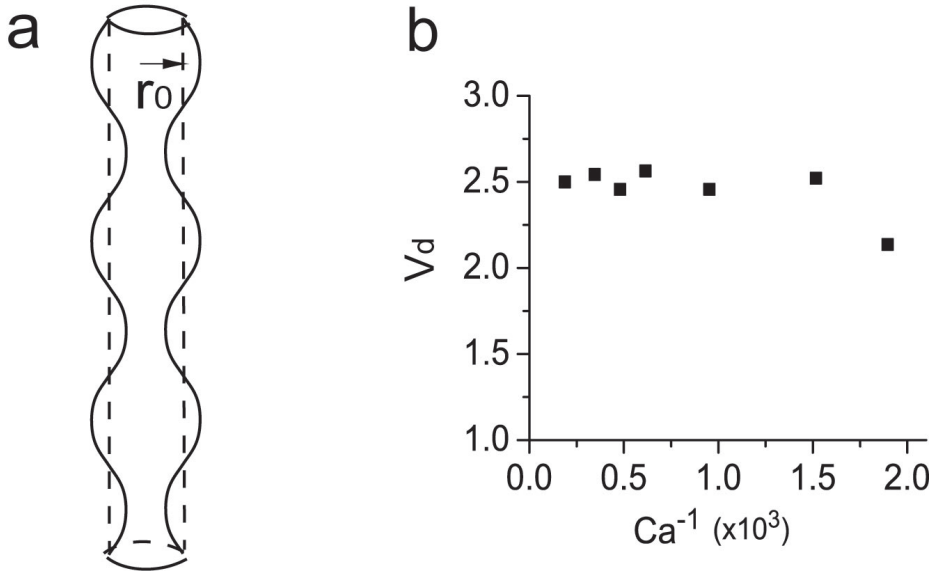

Figure 6.2: (a) Rayleigh-Plateau instability. Perturbations in the form of $\varepsilon coskz$ ($k < 1/r_0$) reduces the surface area, which makes the liquid jet unstable. (b) V_d is independent on C_a^{-1}. The data was collected with the same pressure on both liquid phases. The independence excludes the competence of viscosity and surface tension, which predicts $D \sim C_a^{-1}$, as the droplet breakup mechanism.

To elucidate the mechanism of droplet formation, we measured the volume of

droplets at different flow rates of the two liquid phases. We found the volume of droplets does not depend on the capillary number C_a ($C_a \sim 10^{-4} - 10^{-3}$) (Fig. 6.2b), which clearly indicates a new mechanism of droplet formation for the system.

Without surface instability and with the flow velocity of fluids ($u \leq 1m/s$) being much smaller than the interface relaxation velocity of sound ($\sim 1000m/s$), the system can be considered to be in a quasiequilibrium state [155]. As the tip of the aqueous stream blocks the downstream channel, a pressure difference builds up between the two phases, and the oil starts to accumulate at the junction. This process is quasistatic, so there is direct correlation between the volume of the oil at the junction (grey shade, Fig. 6.3a) and the width of the pinch. Because the hydraulic pressure among each phase does not change much across the junction, the radius of the curvature r of the pinch should be uniform. The volume of oil in the junction can be calculated as

$$V_{oil} = \frac{1}{2}\pi p - \int_0^p 2\pi(h + r - \sqrt{r^2 - x^2})^2 dx, \tag{6.2}$$

where $r = \frac{p^2+b^2}{2b}$. Figure 6.3b shows the calculated V_{oil} at different values of radius of the pinch h. When the oil volume reaches a critical value V_c, where $V_c \leq V_{oil}$, h is sufficiently small, so that surface instability can develop and cause the breakup of the droplet. The time for this instability-driven breakup is short compared to the total time for the droplet formation ($\sim 10^{-3}sec$). The characteristic breakup time caused by surface instability is $(\rho R_0^3/\sigma)^{1/2}$, where ρ is the density of the liquid, and R_0 is radius of the jet. With $\rho \sim 10^3 kg/m^3$, $R_0 \sim 10\mu m$, and $\sigma \sim 10mN/m$, the breakup time is on the order of $10^{-5}sec$. The liquid flowing down the pinch during the short

period of breakup is negligible, and the volume of the droplet is mainly determined by the quasistatic squeezing process.

The total volume of a droplet V_d is the sum of two parts: the volume of aqueous liquid that flows down the pinching position before the pinch forms (V_1) and after the pinch forms (V_2). The flow rates Q_d and Q_c can be considered as constant because the perturbation of the pressure field at the junction is negligible: the fluctuation of surface-tension pressure ($\sim \sigma/w$) during the cycle of droplet formation is small compared to the air pressure at the inlets. V_2 can be calculated as $V_c Q_d/Q_c$. The total volume of a droplet volume then is

$$V_d = V_1 + V_c \frac{Q_d}{Q_c}. \tag{6.3}$$

Figure 6.3c shows the measurement of V_d at different flow rate ratios, Q_d/Q_c. The data was fitted well to Eq. (6.3), yielding critical volume $V_c = 1.80$.

6.2.3 The Role of Liquid Properties and Chip Geometry

According to the Eq. (6.3), the volume of droplets should not depend on the properties of the aqueous phase. To test this, we used water, NEB Buffer 2, and 40% w/w glycerol as the aqueous phase. Indeed, our measurements yielded the same linearity for the three solutions (Fig. 6.4a). Viscosity of water and 40% glycerol differ by ~ 4 fold, with the specific value at $1.0 mPa \cdot s$ and $3.7 mPa \cdot s$, whereas NEB Buffer 2 has somewhat smaller surface tension because salt ions in the buffer disrupt the hydrogen bonding between water molecules. According to Eq. (6.3), volume V_1 and

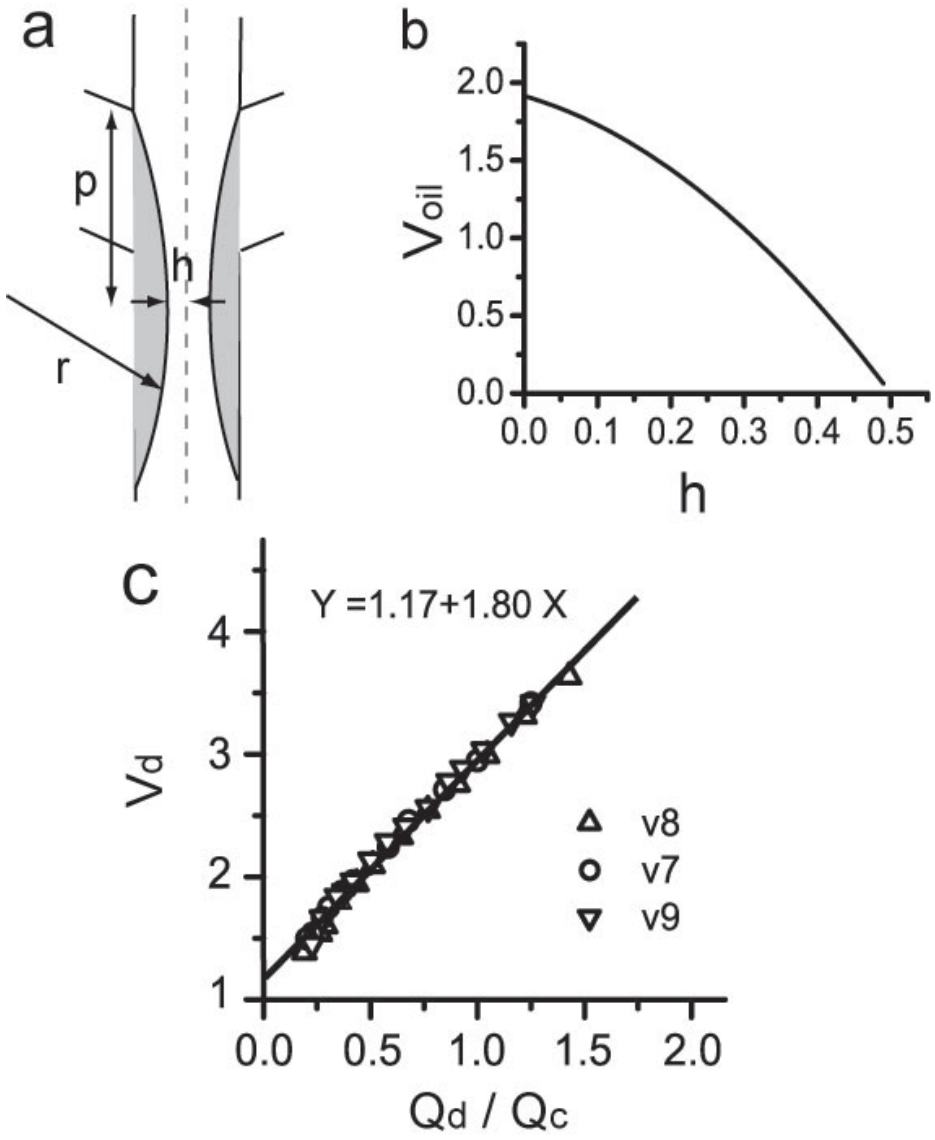

Figure 6.3: (a) The cross-section of a pinch. All the parameters are normalized by the width of the channel. With approximately unchanged during the process, the volume of oil V_{oil} in the junction (grey shade) is only correlated with the radius of the pinch h. (b) Calculated value of V_{oil}. (c) The linear relationship between V_d and the ratio Q_d/Q_c, where Q_d and Q_c are the flow rates of the aqueous phase and the oil phase, respectively. The relationship is the same for different absolute velocity in the common channel. The three sets of data were fitted to Eq. 6.3 together, with $V_1 = 1.17$, and $V_c = 1.80$.

V_c apparently should depend on the geometry of the junction. We made chips with different junction geometry (narrow, normal, and wide) and measured the volume of droplets formed in these chips (Fig. 6.4b). For all three chips, the volume of the droplets is linear to the ratio of flow rates, Q_d/Q_c, but with different sets of linearity constants. Fitting the data to Eq. (6.3) yields a proportionality constant of 1.42, 1.78, and 2.01 and a y-intercept of 0.63, 1.06, and 2.10 for the narrow, normal, and wide chip, respectively. The trend of larger proportionality constant and minimal volume for larger junction is consistent with the model.

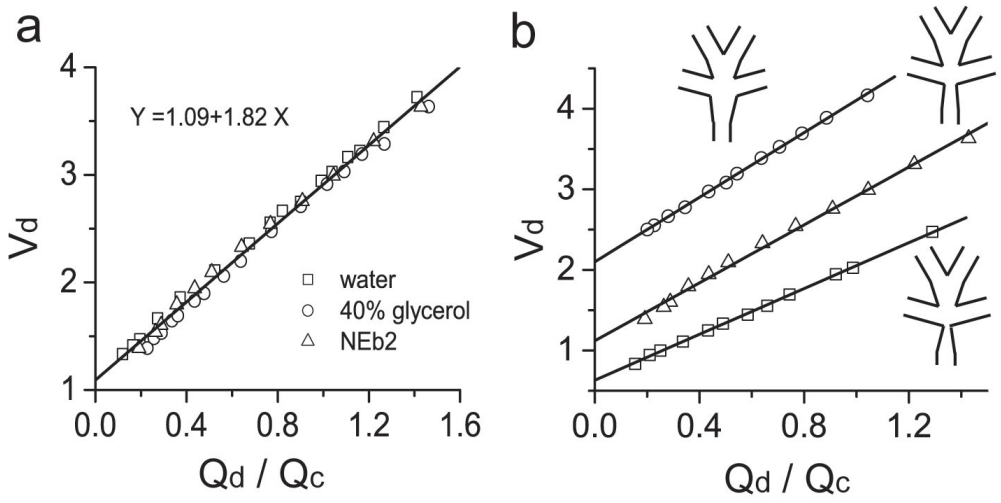

Figure 6.4: Effects of fluid properties and junction geometry on droplet formation. (a) Droplet formation has minimal dependence on fluid properties of the aqueous fluid. NEB buffer 2, 40% glycerol, and water have close fitting parameters (V_1 and V_c). (b) Linearity between V_d and Q_d/Q_c for chips with different junction geometry (wide, normal, and narrow). The three sets of data were fitted to Eq. 6.3, with larger opening geometry resulting in larger fitting parameters, which is in agreement with the model.

6.3 Conclusions

Using a microfluidic chip, one can control the droplet size by monitoring the flow rates and by changing the geometry of the junction. It is know that surface tension, for example, can fluctuation due to temperature change, contamination, and surfactant packaging under dynamic conditions [156]. With the independence on the liquid properties, these fluctuations do not propagate to the droplet volume, ensuring the formation of highly monodipersed droplets. The facility to precisely control droplet formation, together with the capability of droplet manipulation (transportation, isolation, merging, or splitting) with microfluidic devices [143, 157], will make possible a range of new applications that are beyond traditional emulsions.

Bibliography

[1] Watson J.D. and Crick F.H.C. A structure for deoxyribose nucleic acid. *Nature*, 171(4356):737, 1953.

[2] Wilkins M.H.F., A.R. Stokes A.R., and H.R. Wilson. Molecular structure of deoxypentose nucleic acids. *Nature*, 171(4356):738, 1953.

[3] Franklin R. and Gosling R.G. Molecular configuration in sodium thymonucleate. *Nature*, 171(4356):740, 1953.

[4] C.D. Allis, T. Jenuwein, D. Reinberg, and M. L. Caparros. *Epigenetics*. Cold Spring Harbor Laboratory Press, first edition.

[5] RD Kornberg. Chromatin structure: a repeating unit of histones and DNA. *Science*, 184(139):868–71, 1974.

[6] A.L. Olins and D.E. Olins. Spheroid Chromatin Units (ngr Bodies). *Science*, 183(4122):330, 1974.

[7] P.J.J. Robinson, L. Fairall, V.A.T. Huynh, and D. Rhodes. EM measurements define the dimensions of the 30-nm chromatin fiber: Evidence for a compact, interdigitated structure. *Proceedings of the National Academy of Sciences*, 103(17):6506–6511, 2006.

[8] T. Schalch, S. Duda, D.F. Sargent, and T.J. Richmond. X-ray structure of a tetranucleosome and its implications for the chromatin fibre. *Nature*, 436(7047):138–141, 2005.

[9] Ahmet Yildiz, Joseph N. Forkey, Sean A. McKinney, Taekjip Ha, Yale E. Goldman, and Paul R. Selvin. Myosin v walks hand-over-hand: Single fluorophore imaging with 1.5-nm localization. *Science*, 300(5628):2061, 2003.

[10] Ahmet Yildiz, Michio Tomishige, Ronald D. Vale, and Paul R. Selvin. Kinesin walks hand-over-hand. *Science*, 303(5658):676, 2004.

[11] Comert Kural, Hwajin Kim, Sheyum Syed, Gohta Goshima, Vladimir I. Gelfand, and Paul R. Selvin. Kinesin and dynein move a peroxisome in vivo: A tug-of-war or coordinated movement? *Science*, 308(5727):1469, 2005.

[12] Matthew P. Gordon, Taekjip Ha, and Paul R. Selvin. Single-molecule high-resolution imaging with photobleaching. *Proceedings of the National Academy of Sciences*, 101(17):6462, 2004.

[13] Xiaohui Qu, David Wu, Laurens Mets, and Norbert F. Scherer. Nanometer-localized multiple single-molecule fluorescence microscopy. *Proceedings of the National Academy of Sciences*, 101(31):11298, 2004.

[14] L. Stirling Churchman, Zeynep Ökten, Ronald S. Rock, John F. Dawson, and James A. Spudich. Single molecule high-resolution colocalization of cy3 and cy5 attached to macromolecules measures intramolecular distances through time. *Proceedings of the National Academy of Sciences*, 102(5):1419, 2005.

[15] Volker Westphal and Stefan W. Hell. Nanoscale resolution in the focal plane of an optical microscope. *Physical Review Letters*, 94:143903, 2005.

[16] Mats G. L. Gustafsson. Nonlinear structured-illumination microscopy: Wide-field fluorescence imaging with theoretically unlimited resolution. *Proceedings of the National Academy of Sciences*, 102(37):13081, 2005.

[17] Eric Betzig, George H. Patterson, Rachid Sougrat, O. Wolf Lindwasser, Scott Olenych, Juan S. Bonifacino, Michael W. Davidson, Jennifer Lippincott-Schwartz, and Harald F. Hess. Imaging intracellular fluorescent proteins at nanometer resolution. *Science*, 313(5793):1642, 2006.

[18] M. J. Rust, M. Bates, and X. Zhuang. Sub-diffraction-limit imaging by stochastic optical reconstruction microscopy (storm). *Nature Methods*, 3(10):793, 2006.

[19] M. A. Paesler and P. J. Moyer. *Near-field optics.* John Wiley & Sons, first edition.

[20] E.H. Synge. A suggested method for extending the microscopic resolution into the ultramicroscopic region. *Philosophical Magazine*, 6:356, 1928.

[21] D. W. Pohl, W. Denk, and M. Lanz. Optical stethoscopy: Image recording with resolution $\lambda/20$. *Applied Phyics Letters*, 44(7):651, 1984.

[22] A. Lewis, M. Isaacson, A. Harootunian, and A. Murray. Development of a 500 å spatial resolution light microscope. *Ultramicroscopy*, 13(3):227, 1984.

[23] Bert Hecht, Beate Sick, Urs P. Wild, Volker Deckert, Renato Zenobi, Olivier J. F. Martin, and Dieter W. Pohl. Scanning near-field optical microscopy with aperture probes: Fundamentals and applications. *The Journal of Chemical Physics*, 112(18):7761, 2000.

[24] H. A. Bethe. Theory of diffraction by small holes. *The Physical Review*, 66(7/8):163, 1944.

[25] F. Zenhausern, Y. Martin, and H. K. Wickramasinghe. Scanning interferometric apertureless microscopy: Optical imaging at 10 angstrom resolution. *Science*, 269(5227):1083, 1995.

[26] R. Hillenbrand and F. Keilmann. Material-specific mapping of metal/semiconductor/dielectric nanosystems at 10 nm resolution by backscattering near-field optical microscopy. *Applied Physics Letters*, 80(1):25, 2002.

[27] A. Hartschuh, E. J. Sánchez, X. S. Xie, and L. Novotny. High-resolution near-field raman microscopy of single-walled carbon nanotubes. *Physical Review Letters*, 90(9):095503, 2003.

[28] T. Ichimura, N. Hayazawa, M. Hashimoto, Y. Inouye, and S. Kawata. Tip-enhanced coherent anti-stokes raman scattering for vibrational nanoimaging. *Physical Review Letters*, 92(22):220801, 2004.

[29] E. J. Sánchez, L. Novotny, and X. S. Xie. Near-field fluorescence microscopy based on two-photon excitation with metal tips. *Physical Review Letters*, 82(20):4014, 1999.

[30] J. M. Gerton, L. A. Wade, G. A. Lessard, Z. Ma, and S. R. Quake. Tip-enhanced fluorescence microscopy at 10 nm resolution. *Physical Review Letters*, 93(18):180801, 2004.

[31] H. F. Hamann, M. Kuno, A. Gallagher, and D. J. Nesbitt. Molecular fluorescence in the vicinity of a nanoscopic probe. *Journal of Chemical Physics*, 114(19):8596, 2001.

[32] T. J. Yang, G. A. Lessard, and S. R. Quake. An apertureless near-field microscope for fluorescence imaging. *Applied Physics Letters*, 76(3):378, 2000.

[33] H. F. Hamann, A. Gallagher, and D. J. Nesbitt. Enhanced sensitivity near-field scanning optical microscopy at high spatial resolution. *Applied Physics Letters*, 73(11):1469, 1998.

[34] V. V. Protasenko, M. Kuno, A. Gallagher, and D. J. Nesbitt. Fluorescence of single zns overcoated cdse quantum dots studied by apertureless near-field scanning optical microscopy. *Optics Communications*, 210(1-2):11, 2002.

[35] V. V. Protasenko, A. Gallagher, and D. J. Nesbitt. Factors that influence confocal apertureless near-field scanning optical microscopy. *Optics Communications*, 233(1-3):45, 2004.

[36] E. Betzig and R. J. Chichester. Single molecules observed by near-field scanning optical microscopy. *Science*, 262(5138):1422, 1993.

[37] H. G. Frey, S. Witt, K. Felderer, and R. Guckenberger. High-resolution imaging of single fluorescent molecules with the optical near-field of a metal tip. *Physical Review Letters*, 93(20):200801, 2004.

[38] V. V. Protasenko and A. C. Gallagher. Apertureless near-field scanning optical microscopy of single molecules. *Nano Letters*, 4(7):1329, 2004.

[39] J.M. Gerton, L.A. Wade, G.A. Lessard, Z. Ma, and S.R. Quake. Tip-Enhanced Fluorescence Microscopy at 10 Nanometer Resolution. *Physical Review Letters*, 93(18):180801, 2004.

[40] Z. Ma, J.M. Gerton, L.A. Wade, and S.R. Quake. Fluorescence Near-Field Microscopy of DNA at Sub-10 nm Resolution. *Physical Review Letters*, 97(26):260801, 2006.

[41] L. Novotny, R. X. Bian, and X. S. Xie. Theory of nanometric optical tweezers. *Physical Review Letters*, 79(4):645, 1997.

[42] L. Aigouy, A. Lahrech, S. Grsillon, H. Cory, A. C. Boccara, and J. C. Rivoal. Polarization effects in apertureless scanning near-field optical microscopy: an experimental study. *Optics Letters*, 24(4):187, 1999.

[43] B. Sick, B. Hecht, U. P. Wild, and L. Novotny. Probing confined fields with single molecules and vice versa. *Journal of Microscopy*, 202(2):365, 2001.

[44] G. A. Lessard. *Apertureless Near-Field Optcial Microscopy for Fluorescence Imaging*. PhD thesis, California Institute of Technology, 2003.

[45] J. A. Stratton. *Electromagnetic Theory*. McGraw-Hill, first edition.

[46] S. Kawata (Ed.). *Near-Field Optics and Surface Plasmon Polaritons*. Springer, first edition.

[47] A. Bouhelier, M. Beversluis, A. Hartschuh, and L. Novotny. Near-field second-harmonic generation induced by local field enhancement. *Physical Review Letters*, 90(1):013903, 2003.

[48] B. Knoll and F. Keilmann. Near-field probing of vibrational absorption for chemical microscopy. *Nature*, 399(6732):134, 1999.

[49] H. G. Frey, F. Keilmann, K. Felderer, and R. Guckenberger. Enhancing the resolution of scanning near-field optical microscopy by a metal tip grown on an aperture probe. *Applied Physics Letters*, 81(26):5030, 2002.

[50] Y. Kawata, C. Xu, and W. Denk. Feasibility of molecular-resolution fluorescence near-field microscopy using multi-photon absorption and field enhancement near a sharp tip. *Journal of Applied Physics*, 85(3):1294, 1999.

[51] J. L. Bohn, D. J. Nesbitt, and A. Gallagher. Field enhancement in apertureless near-field scanning optical microscopy. *Optical Society of America Journal*, 18(12):2998, 2001.

[52] Y. C. Martin, H. F. Hamann, and H. K. Wickramasinghe. Strength of the electric field in apertureless near-field optical microscopy. *Journal of Applied Physics*, 89(10):5774, 2001.

[53] N. F. van Hulst, J. A. Veerman, M. F. Garcí a Paraj ó, and L. K. Kuipers. Analysis of individual (macro)molecules and proteins using near-field optics. *Journal of Chemical Physics*, 112(18):7799, 2000.

[54] R. Dorn, S. Quabis, and G. Leuchs. Sharper focus for a radially polarized light beam. *Physical Review Letters*, 91(23):233901, 2003.

[55] R. G. Neuhauser, K. T. Shimizu, W. K. Woo, S. A. Empedocles, and M. G. Bawendi. Correlation between fluorescence intermittency and spectral diffusion in single semiconductor quantum dots. *Physical Review Letters*, 85(15):3301, 2000.

[56] M. Kuno, D. P. Fromm, H. F. Hamann, A. Gallagher, and D. J. Nesbitt. Non-exponential "blinking" kinetics of single cdse quantum dots: A universal power law behavior. *Journal of Chemical Physics*, 112(7):3117, 2000.

[57] S. Weiss. Fluorescence spectroscopy of single biomolecules. *Science*, 283(5408):1676, 1999.

[58] W. E. Moerner and M. Orrit. Illuminating single molecules in condensed matter. *Science*, 283(5408):1670, 1999.

[59] J. Azoulay, A. Débarre, A. Richard, and P P. Tchénio. Quenching and enhancement of single-molecule fluorescence under metallic and dielectric tips. *Europhysics Letters*, 51(4):374, 2000.

[60] W. Trabesinger, A. Kramer, M. Kreiter, B. Hecht, and U. P. Wild. Single-molecule near-field optical energy transfer microscopy with dielectric tips. *Journal of Microscopy*, 209(3):249, 2003.

[61] W. Trabesinger, A. Kramer, M. Kreiter, B. Hecht, and U. P. Wild. Single-molecule near-field optical energy transfer microscopy with dielectric tips. *Applied Physics Letters*, 81(11):2118, 2002.

[62] P. J. Schuck, D. P. Fromm, A. Sundaramurthy, G. S. Kino, and W. E. Moerner. High-resolution imaging of single fluorescent molecules with the optical near-field of a metal tip. *Physical Review Letters*, 94(1):017402, 2005.

[63] P. Mühlschlegel, H. J. Eisler, O. J. F. Martin, B. Hecht, and D. W. Pohl. Resonant optical antennas. *Science*, 308(5728):1607, 2005.

[64] J. N. Farahani, D. W. Pohl, H. J. Eisler, and B. Hecht. Single quantum dot coupled to a scanning optical antenna: A tunable superemitter. *Physical Review Letters*, 95(1):017402, 2005.

[65] F. J. Giessibl. Advances in atomic force microscopy. *REVIEWS OF MODERN PHYSICS*, 75(3):949, 2003.

[66] H. G. Hansma, I. Revenko, K. Kim, and D. E. Laney. Atomic force microscopy of long and short double-stranded, single- stranded and triple-stranded nucleic acids. *Nucleic Acids Research*, 24(4):713, 1996.

[67] D. G. Norman, R. J. Grainger, D. Uhrín, and D. M. J. Lilley. Location of cyanine-3 on double-stranded dna: Importance for fluorescence resonance energy transfer studies. *Biochemistry*, 39(21):6317, 2000.

[68] R. E. Franklin and R.G. Gosling. Molecular configuration in sodium thmonucleate. *Nature*, 171(7):740, 1953.

[69] X. J. Lu, Z. Shakked, and W. K. Olson. A-form conformational motifs in ligand-bound dna structures. *Jounal of Molecular Biology*, 300(4):819, 2000.

[70] S. B. Zimmerman. The three-dimensional structure of dna. *Annual Review of Biochemistry*, 51:4014, 1982.

[71] X. J. Lu and W. K. Olson. 3dna: a software package for the analysis, rebuilding and visualization of three-dimensional nucleic acid structures. *Nucleic Acids Research*, 31(17):5108, 2003.

[72] Z. Shakked, G. Guerstein-Guzikevich, M. Eisenstein, F. Frolow, and D. Rabinovich. The conformation of the dna double helix in the crystal is dependent on its environment. *Nature*, 342(6248):456, 1989.

[73] J. Hafner, C.L. Cheung, T.H. Oosterkamp, and C.M. Lieber. High-yield assembly of individual single-walled carbon nanotube tips for scanning probe microscopies. *Journal of Physical Chemistry B*, 105(4):743, 2001.

[74] L.A. Wade, I.R. Shapiro, Z. Ma, S.R. Quake, and C.P. Collier. Correlating afm probe morphology to image resolution for single-wall carbon nanotube tips. *Nano Letters*, 4(4):725, 2004.

[75] T. Sulchek, R. Hsieh, J. D. Adams, S. C. Minne, C. F. Quate, and D. M. Adderton. High-speed atomic force microscopy in liquid. *Review of Scientific Instruments*, 71(5):2097, 2000.

[76] JH Hafner, CL Cheung, AT Woolley, and CM Lieber. Structural andfunctional imaging with carbon nanotube AFM probes. *Progress in Biophysics & Molecular Biology*, 77:73–110, 2001.

[77] S.S. Wong, J.D. Harper, P.T. Lansbury Jr, and C.M. Lieber. Carbon Nanotube Tips: High-Resolution Probes for Imaging Biological Systems. *Journal of the American Chemical Society*, 120:603–604, 1998.

[78] SS Wong, AT Woolley, TW Odom, JL Huang, P. Kim, DV Vezenov, and CM Lieber. Single-walled carbon nanotubeprobesforhigh-resolutionnanostructureimaging. *Appl. Phys. Lett*, 73:3465–3467.

[79] A. Krishnan, E. Dujardin, TW Ebbesen, PN Yianilos, and MMJ Treacy. Youngs modulus of single-walled nanotubes. *Physical Review B*, 58(20):14013–14019, 1998.

[80] E.W. Wong, P.E. Sheehan, and C.M. Lieber. Nanobeam Mechanics: Elasticity, Strength, and Toughness of Nanorods and Nanotubes. *Science*, 277(5334):1971–1975, 1997.

[81] T. Larsen, K. Moloni, F. Flack, M.A. Eriksson, M.G. Lagally, and C.T. Black. Comparison of wear characteristics of etched-silicon and carbon nanotube atomic-force microscopy probes. *Applied Physics Letters*, 80(11):1996, 2002.

[82] S.S. Wong, E. Joselevich, A.T. Woolley, C.L. Cheung, and C.M. Lieber. Covalently functionalized nanotubesasnanometre-sizedprobesin chemistryandbiology. *NATURE*, 394:53, 1998.

[83] H. Dai, J.H. Hafner, A.G. Rinzler, D.T. Colbert, and R.E. Smalley. Nanotubes as nanoprobes in scanning probe microscopy. *Nature*, 384(6605):147–150, 1996.

[84] EB Cooper, SR Manalis, H Fang, H Dai, SC Minne, T Hunt, and CF Quate. Terabit-per-square-inch data storage with the atomic force microscope. *Applied Physics Letters*, 75(22):3566, 1999.

[85] J.H. Hafner, C.L. Cheung, and C.M. Lieber. Direct Growth of Single-Walled Carbon Nanotube Scanning Probe Microscopy Tips. *Journal of the American Chemical Society*, 121:9750, 1999.

[86] J.H. Hafner, C.L. Cheung, and C.M. Lieber. Growth of nanotubes for probe microscopy tips. *Nature*, 398(6730):761, 1999.

[87] Y. Li, W. Kim, Y. Zhang, M. Rolandi, D. Wang, and H. Dai. Growth of single-walled carbon nanotubes from discrete catalytic nanoparticles of various sizes. *Journal of Physical Chemistry B*, 105(46):11424–11431, 2001.

[88] I.R. Shapiro, S. Solares, M.J. Esplandiu, L.A. Wade, W.A. Goddard, and C.P. Collier. Influence of elastic deformation on single-wall carbon nanotube atomic force microscopy probe resolution. *Journal of Physical Chemistry B*, 108(36):13613–13618, 2004.

[89] H.W.C. Postma, A. Sellmeijer, and C. Dekker. Manipulation and Imaging of Individual Single-Walled Carbon Nanotubes with an Atomic Force Microscope. *Advanced Materials*, 12(17):1299–1302, 2000.

[90] ES Snow, PM Campbell, and JP Novak. Single-wall carbon nanotube atomic force microscope probes. *Applied Physics Letters*, 80:2003, 2002.

[91] C.L. Cheung, J.H. Hafner, and C.M. Lieber. Carbon nanotube atomic force microscopy tips: Direct growth by chemical vapor deposition and application to high-resolution imaging. 97(8):3809–3813, 2000.

[92] B.I. Yakobson and P. Avouris. Mechanical properties of carbon nanotubes. *Topics in Applied Physics*, 80:287–327, 2001.

[93] U. Hubscher, G. Maga, and S. Spadari. Eukaryotic DNA polymerases. *Annu. Rev. Biochem.*, 71:133–63, 2002.

[94] D.K. Braithwaite and J. Ito. Compilation, alignment, and phylogenetic relationships of DNA polymerases. *Nucleic Acids Research*, 21(4):787–802, 1993.

[95] M. Delarue, O. Poch, N. Tordo, D. Moras, and P. Argos. An attempt to unify the structure of polymerases. *Protein Engineering Design and Selection*, 3:461–467, 1990.

[96] T.A. Steitz. DNA Polymerases: Structural Diversity and Common Mechanisms. *Journal of Biological Chemistry*, 274(25):17395–17398, 1999.

[97] RD Kuchta, V. Mizrahi, PA Benkovic, KA Johnson, and SJ Benkovic. Kinetic mechanism of DNA polymerase I (Klenow). *Biochemistry*, 26(25):8410–8417, 1987.

[98] R.D. Kuchta, P. Benkovic, and S.J. Benkovic. Kinetic mechanism whereby DNA polymerase I (Klenow) replicates DNA with high fidelity. *Biochemistry*, 27(18):6716–6725, 1988.

[99] S.S. Patel, I. Wong, and K.A. Johnson. Pre-steady-state kinetic analysis of processive DNA replication including complete characterization of an exonuclease-deficient mutant. *Biochemistry*, 30(2):511–525, 1991.

[100] T.L. Capson, J.A. Peliska, B.F. Kaboord, M.W. Frey, C. Lively, M. Dahlberg, and S.J. Benkovic. Kinetic characterization of the polymerase and exonuclease activities of the gene 43 protein of bacteriophage T4. *Biochemistry*, 31(45):10984–10994, 1992.

[101] B.G. Werneburg, J. Ahn, X. Zhong, R.J. Hondal, V.S. Kraynov, and M.D. Tsai. DNA polymerase β: pre-steady-state kinetic analysis and roles of arginine-283 in catalysis and fidelity. *Biochemistry*, 35(22):7041–7050, 1996.

[102] M.T. Washington, L. Prakash, and S. Prakash. Yeast DNA Polymerase η Utilizes an Induced-Fit Mechanism of Nucleotide Incorporation. *Cell*, 107(7):917–927, 2001.

[103] WM Kati, KA Johnson, LF Jerva, and KS Anderson. Mechanism and fidelity of HIV reverse transcriptase. *Journal of Biological Chemistry*, 267(36):25988–25997, 1992.

[104] T.A. Kunkel. DNA Replication Fidelity. *Journal of Biological Chemistry*, 279(17):26895–26898, 2004.

[105] W.A. Beard and S.H. Wilson. Structural insights into the origins of DNA polymerase fidelity. *Structure*, 11(5), 2003.

[106] S. Doublié, S. Tabor, A.M. Long, C.C. Richardson, and T. Ellenberger. Crystal structure of a bacteriophage T7 DNA replication complex at 2.2 Å resolution. *Nature*, 391:251–258, 1998.

[107] S. Doublié, M.R. Sawaya, and T. Ellenberger. An open and closed case for all polymerases. *Structure*, 7(2):31–35, 1999.

[108] S.H. Eom, J. Wang, and T.A. Steitz. Structure of Taq polymerase with DNA at the polymerase active site. *Nature*, 382(6588):278–281, 1996.

[109] Y. Li, S. Korolev, and G. Waksman. Crystal structures of open and closed forms of binary and ternary complexes of the large fragment of Thermus aquaticus DNA polymerase I: structural basis for nucleotide incorporation. *The EMBO Journal*, 17:7514–7525, 1998.

[110] LV Mendelman, MS Boosalis, J. Petruska, and MF Goodman. Nearest neighbor influences on DNA polymerase insertion fidelity. *Journal of Biological Chemistry*, 264(24):14415–14423, 1989.

[111] L.B. Bloom, M.R. Otto, J.M. Beechem, and M.F. Goodman. Influence of 5'-nearest neighbors on the insertion kinetics of the fluorescent nucleotide analog 2-aminopurine by Klenow fragment. *Biochemistry*, 32(41):11247–11258, 1993.

[112] Z. Wang, E. Lazarov, M. O'Donnell, and M.F. Goodman. Resolving a Fidelity Paradox: Why *Echerichia Coli* DNA Polymerase II Makes More Base Substitution Errors in AT- Compared with GC-Rich DNA. *Journal of Biological Chemistry*, 277(6):4446–4454, 2002.

[113] W.A. Beard, D.D. Shock, and S.H. Wilson. Influence of DNA Structure on DNA Polymerase β Active Site Function. *Journal of Biological Chemistry*, 279(30):31921–31929, 2004.

[114] Y. Xia and G.M. Whitesides. Soft lithography. *Angew Chem. Int. Ed*, 37(5):550–75, 1998.

[115] H. Song and R.F. Ismagilov. Millisecond kinetics on a microfluidic chip using nanoliters of reagents. *J. Am. Chem. Soc*, 125(14):613, 2003.

[116] H. Song, JD Tice, and RF Ismagilov. A microfluidic system for controlling reaction networks in time. *Angew Chem. Int. Ed.*, 42(7):768–72, 2003.

[117] V. Purohit, ND Grindley, and C.M. Joyce. Use of 2-aminopurine fluorescence to examine conformational changes during nucleotide incorporation by DNA polymerase I (Klenow fragment). *Biochemistry*, 42(34):10200–10211, 2003.

[118] I. Wong, S.S. Patel, and K.A. Johnson. An induced-fit kinetic mechanism for DNA replication fidelity: direct measurement by single-turnover kinetics. *Biochemistry*, 30(2):526–537, 1991.

[119] T.A. Kunkel and S.H. Wilson. DNA polymerases on the move. *Nature Structural Biology*, 5:95–99, 1998.

[120] R.A. Friedman and B. Honig. A free energy analysis of nucleic acid base stacking in aqueous solution. *Biophysical Journal*, 69(4):1528–1535, 1995.

[121] A.M. Shah, S.X. Li, K.S. Anderson, and J.B. Sweasy. Y265H Mutator Mutant of DNA Polymerase β: Proper Geometric Alignment is Critical for Fidelity. *Journal of Biological Chemistry*, 276(14):10824–10831, 2001.

[122] X. Zhong, SS Patel, and MD Tsai. DNA polymerase β. 5. Dissecting the functional roles of the two metal ions with Cr (III) dTTP. *Journal of the American Chemical Society*, 120(1):235–236, 1998.

[123] B.J. Vande Berg, W.A. Beard, and S.H. Wilson. DNA Structure and Aspartate 276 Influence Nucleotide Binding to Human DNA Polymerase β: Implication for

the Identity of the Rate-limting Conformational Change. *Journal of Biological Chemistry*, 276(5):3408–3416, 2001.

[124] J.W. Arndt, W. Gong, X. Zhong, A.K. Showalter, J. Liu, C.A. Dunlap, Z. Lin, C. Paxson, M.D. Tsai, and M.K. Chan. Insight into the catalytic mechanism of DNA polymerase beta: structures of intermediate complexes. *Biochemistry*, 40(18):5368–75, 2001.

[125] P.J. Rothwell, V. Mitaksov, and G. Waksman. Motions of the Fingers Subdomain of Klentaq1 Are Fast and Not Rate Limiting: Implications for the Molecular Basis of Fidelity in DNA Polymerases. *Mol. Cell*, 19:345–355, 2005.

[126] G. Luo, M. Wang, W. H. Konigsberg, and X. S. Xie. Single-molecule and ensemble fluorescence assays for a functionally important conformational change in T7 DNA polymerase. *Proceedings of the National Academy of Science*, 104:12610–12615, 2007.

[127] M. Bakhtina, M.P. Roettger, S. Kumar, and M.D. Tsai. A Unified Kinetic Mechanism Applicable to Multiple DNA Polymerases. *Biochemistry*, 46(18):5463–5472, 2007.

[128] V.K. Batra, W.A. Beard, D.D. Shock, J.M. Krahn, L.C. Pedersen, and S.H. Wilson. Magnesium-induced assembly of a complete DNA polymerase catalytic complex. *Structure*, 14(4):757–766, 2006.

[129] L.A. Loeb and B.D. Preston. Mutagenesis by Apurinic/Apyrimidinic Sites. *Annual Review of Genetics*, 20(1):201–230, 1986.

[130] JM Clark, CM Joyce, and GP Beardsley. Novel blunt-end addition reactions catalyzed by DNA polymerase I of Escherichia coli. *J Mol Biol*, 198(1):123–7, 1987.

[131] TJ Matray and ET Kool. A specific partner for abasic damage in DNA. *Nature*, 399(6737):704–8, 1999.

[132] J. Cline, JC Braman, and HH Hogrefe. PCR fidelity of pfu DNA polymerase and other thermostable DNA polymerases. *Nucleic Acids Research*, 24(18):3546–3551, 1996.

[133] M. Ronaghi. Pyrosequencing Sheds Light on DNA Sequencing. 11(1):3–11, 2001.

[134] MC Cross and PC Hohenberg. Pattern formation outside of equilibrium. *Reviews of Modern Physics*, 65(3):851–1112, 1993.

[135] T. Thorsen, R.W. Roberts, F.H. Arnold, and S.R. Quake. Dynamic Pattern Formation in a Vesicle-Generating Microfluidic Device. *Physical Review Letters*, 86(18):4163–4166, 2001.

[136] R. Dreyfus, P. Tabeling, and H. Willaime. Ordered and Disordered Patterns in Two-Phase Flows in Microchannels. *Physical Review Letters*, 90(14):144505, 2003.

[137] T. Nisisako, T. Torii, and T. Higuchi. Droplet formation in a microchannel network. *Lab Chip*, 2(1):24–26, 2002.

[138] S.L. Anna, N. Bontoux, and H.A. Stone. Formation of dispersions usingflow focusing in microchannels. *Applied Physics Letters*, 82(3):364, 2003.

[139] J.D. Tice, H. Song, A.D. Lyon, and R.F. Ismagilov. Formation of droplets and mixing in multiphase microfluidics at low values of the Reynolds and the capillary numbers. *Langmuir*, 19(22):9127–9133, 2003.

[140] B. Zheng, L.S. Roach, and R.F. Ismagilov. Screening of protein crystallization conditions on a microfluidic chip using nanoliter-size droplets. *J Am Chem Soc*, 125(37):11170–11171, 2003.

[141] B. Zheng, J.D. Tice, and R.F. Ismagilov. Formation of Arrayed Droplets by Soft Lithography and Two-Phase Fluid Flow, and Application in Protein Crystallization. *Advanced Materials*, 16(15):1365–1368, 2004.

[142] B. Zheng, J.D. Tice, L.S. Roach, and R.F. Ismagilov. A Droplet-Based, Composite PDMS/Glass Capillary Microfluidic System for Evaluating Protein Crystallization Conditions by Microbatch and Vapor-Diffusion Methods with On-Chip X-Ray Diffraction. *Angewandte Chemie International Edition*, 43(19):2508–2511, 2004.

[143] L.H. Hung, K.M. Choi, W.Y. Tseng, Y.C. Tan, K.J. Shea, and A.P. Lee. Alternating droplet generation and controlled dynamic droplet fusion in microfluidic device for CdS nanoparticle synthesis. *Lab Chip*, 6:174–178, 2006.

[144] B.T.C. Lau, C.A. Baitz, X.P. Dong, and C.L. Hansen. A complete microfluidic screening platform for rational protein crystallization. *Journal of the American Chemical Society*, 129(3):454–455, 2007.

[145] M.J. Fuerstman, P. Garstecki, and G.M. Whitesides. Coding/Decoding and Reversibility of Droplet Trains in Microfluidic Networks. *Science*, 315(5813):828, 2007.

[146] L.F. Cheow, L. Yobas, and D.L. Kwong. Digital microfluidics: Droplet based logic gates. *Applied Physics Letters*, 90:054107, 2007.

[147] M. Prakash and N. Gershenfeld. Microfluidic Bubble Logic. *Science*, 315(5813):832, 2007.

[148] GI Taylor. The Formation of Emulsions in Definable Fields of Flow. *Proceedings of the Royal Society of London. Series A, Containing Papers of a Mathematical and Physical Character*, 146(858):501–523, 1934.

[149] V. Cristini and Y.C. Tan. Theory and numerical simulation of droplet dynamics in complex flowsa review. *Lab Chip*, 4:257–264, 2004.

[150] JH Xu, GS Luo, SW Li, and GG Chen. Shear force induced monodisperse droplet formation in a microfluidic device by controlling wetting properties. *Lab Chip*, 6:131–136, 2006.

[151] J.D. Tice, A.D. Lyon, and R.F. Ismagilov. Effects of viscosity on droplet formation and mixing in microfluidic channels. *Analytica Chimica Acta*, 507(1):73–77, 2004.

[152] B.J. Adzima and S.S. Velankar. Pressure drops for droplet flows in microfluidic channels. *Journal of Micromechanics and Microengineering*, 16(8):1504–1510, 2006.

[153] P. Garstecki, M.J. Fuerstman, H.A. Stone, and G.M. Whitesides. Formation of droplets and bubbles in a microfluidic T-junctionscaling and mechanism of break-up. *Lab Chip*, 6:437–446, 2006.

[154] A. Liau, R. Karnik, A. Majumdar, and J.H.D. Cate. Mixing Crowded Biological Solutions in Milliseconds. *Anal. Chem*, 77(23):7618–7625, 2005.

[155] P. Garstecki, H.A. Stone, and G.M. Whitesides. Mechanism for Flow-Rate Controlled Breakup in Confined Geometries: A Route to Monodisperse Emulsions. *Physical Review Letters*, 94(16):164501, 2005.

[156] C.D. Eggleton, T.M. Tsai, and K.J. Stebe. Tip Streaming from a Drop in the Presence of Surfactants. *Physical Review Letters*, 87(4):48302, 2001.

[157] DR Link, SL Anna, DA Weitz, and HA Stone. Geometrically Mediated Breakup of Drops in Microfluidic Devices. *Physical Review Letters*, 92(5):54503, 2004.